# Harmonics of lepton-jet correlations in inclusive and diffractive scatterings

Xuan-Bo Tong,[2,3,1,*] Bo-Wen Xiao,[1,†] and Yuan-Yuan Zhang[4,1,‡]

[1]School of Science and Engineering, The Chinese University of Hong Kong, Shenzhen, Shenzhen, Guangdong, 518172, People's Republic of China
[2]Department of Physics, University of Jyväskylä, P.O. Box 35, 40014 University of Jyväskylä, Finland
[3]Helsinki Institute of Physics, P.O. Box 64, 00014 University of Helsinki, Finland
[4]Shandong Institute of Advanced Technology, Jinan 250100, China

(Received 9 November 2023; accepted 17 January 2024; published 4 March 2024)

Based on our previous work, we study the harmonic coefficient of both inclusive and diffractive azimuthal angle dependent lepton-jet correlations in the Hadron-Electron Ring Accelerator and the future electron-ion collider. Numerical calculations for inclusive and diffractive harmonics, and the ratio of harmonics in $e + \mathrm{Au}$ and $e + p$, indicate their strong discriminating power for nonsaturation models and saturation models. Additionally, we demonstrate that the $t$-dependent diffractive harmonics can serve as novel observables for the nuclear density profile.

DOI: 10.1103/PhysRevD.109.054004

## I. INTRODUCTION

In a recent paper [1], we have demonstrated how the harmonics of lepton-jet correlation can serve as a new probe for the saturation phenomenon in deeply inelastic scattering (DIS). In this paper, we present a more detailed elaboration on the harmonics of lepton-jet correlation and extend the discussion to diffractive lepton-jet production.

Gluon saturation [2–7] is a phenomenon observed in the proton/nucleus of high energy collisions. Large-$x$ partons radiate small-$x$ gluons, leading to an increase in the density of small-$x$ gluons. These small-$x$ gluons come into close proximity, interact, and recombine. These two effects compete until the small-$x$ gluon density saturates. The typical transverse momentum associated with saturated gluons is referred to as the saturation scale $Q_s$.

The color glass condensate (CGC) effective theory is the theoretical framework used to describe saturated gluons. In the CGC effective theory, large-$x$ partons are treated as static and localized color sources, while small-$x$ partons are modeled as classical and dynamical fields. The relationship between the sources and fields is governed by the classical Yang-Mills equation. When considering the interaction of an energetic parton with the classical field, lightlike Wilson lines emerge, which resum the multiple interactions between the high energy parton and the classical field. The two-point correlator of a quark wilson line and an antiquark wilson line yields the dipole scattering matrix. The Wilson lines and dipole scattering matrix are the building blocks of small-$x$ physics. More detailed descriptions of the CGC framework can be found in the reviews [8–13].

Two particle correlations, such as dijet [14–47], dihadron [44,48–53], and jet plus color-neutral particle [17,54] have been extensively employed to explore various aspects of saturation in the future electron-ion collider (EIC) [55–59]. These correlations enable investigations into Weizsäcker-Williams gluon distributions [16–28], including the linear polarized one [19,20,22–26,31,32]. Measurement of the unpolarized dipole gluon distribution [16,17] and its linear polarized counterpart [31,32] are also possible. Furthermore, multigluon correlations within the nucleus target can be probed [14,15,29,37], and the Wigner funtion can be investigated within the small-$x$ framework [41,43,48]. The separation of Sudakov resummation and small-$x$ resummation has been elucidated [18,25,27,28,60]. Besides EIC, the two particle correlations have also been extensively discussed in the LHC and RHIC (see, e.g., [16–18,61–109]).

Typically, two-particle correlations exhibit a back-to-back configuration in the transverse plane perpendicular to the beam direction. This configuration, known as the correlation limit, occurs when the imbalance momentum $|\vec{q}_\perp| = |\vec{k}_{1\perp} + \vec{k}_{2\perp}|$ is much softer than the relative momentum $|\vec{P}_\perp| = |(\vec{k}_{1\perp} - \vec{k}_{2\perp})/2|$. In this limit, the soft imbalanced momentum can reach the saturation region $|\vec{q}_\perp| \lesssim Q_s$. Thus, the two particle correlation in the correlation limit serves as a robust probe for saturation.

*xuan.bo.tong@jyu.fi
†xiaobowen@cuhk.edu.cn
‡yuanyuan.zhang@iat.cn

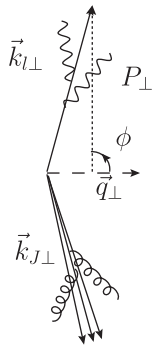


FIG. 1. Lepton jet in the transverse plane, perpendicular to the beam direction. The final jet radiates soft gluons, while the final lepton emits soft photons.

A recent addition to the repertoire of two-particle correlation is the lepton-jet correlation in DIS [110,111]. Figure 1 illustrates the lepton-jet production in the transverse plane, with the final jet radiating gluons and the final lepton emitting photons. Lepton-jet correlation provides a valuable avenue for studying the transverse momentum dependent (TMD) quark distribution, as well as the TMD quark Sivers function [110–117], and the Collins fragmentation function [112–114]. Notably, in the small-$x$ region, the TMD quark distribution within the small-$x$ framework contains critical information about gluon saturation. Consequently, lepton-jet correlation emerges as an opportunity to probe this intriguing phenomenon [1].

Following the theoretical papers on lepton-jet correlation, an increasing number of experimental studies have emerged. The first measurement of lepton-jet correlation at the Hadron-Electron Ring Accelerator (HERA) [118] with the H1 detector has been published [119]. Additionally, event generation and detector-response simulations have been conducted to investigate lepton-jet production at EIC kinematics [112,114,120].

The azimuthal angle anisotropy or harmonics of the lepton-jet correlation serves as observable in the search for gluon saturation. Previous studies have indicated that the azimuthal angle anisotropy is caused by soft gluon radiation [121,122], as soft gluon radiation from the final jet tends to align with the final jet. In the small-$x$ formalism, the initial TMD quark distribution can be seen as arising from dipole-nucleus multiple scattering and small-$x$ gluon radiation in the schematic diagram of the dipole picture. The transverse momentum of the initial quark, which is determined by gluon saturation, does not exhibit a preferred angle. Therefore, gluon saturation tends to suppress the anisotropy.

We calculate the harmonics of the lepton-jet correlation within both the saturation framework and the nonsaturation framework. The saturation framework is based on small-$x$ factorization and resummation [16,17,123–125], while the nonsaturation framework involves TMD factorization [121,122,126,127] with collinear PDFs. As the saturation scale is proportional to the nuclear size, $Q_s^2 \propto A^{1/3}$, with $A$ representing the nucleon number, the suppression of harmonics is more pronounced in large nuclei compared to protons. We observe this effect when comparing the harmonics in protons and gold nuclei.

Motivated by recent papers [39,128], we further study the harmonics of diffractive lepton-jet production in DIS. In the small-$x$ region, diffractive parton distributions [129] are related to the color-dipole S matrix [39,128,130–135], allowing us to probe gluon saturation through DPDFs. For comprehensive overviews and recent progress in diffraction within the dipole picture, refer to reviews [8,136,137] and Refs. [33–45,128,138–165]. Similar to the discussion on semi-inclusive diffractive deep inelastic scattering (SIDDIS) at small-$x$ [128], we expect that QCD factorization also holds for diffractive lepton-jet production. Although the diffractive lepton-jet process is defined in the lepton-nucleon center-of-mass frame, the rapidity gap is nearly the same as the rapidity gap in the photon-nucleon center-of-mass frame $Y_{\mathrm{IP}} \sim \ln(1/x_{\mathrm{IP}})$. We calculate the harmonics for the diffractive process and observe a decrease in harmonics when transitioning from a proton target to a gold target. The $t$-dependent harmonics are found to be sensitive to different nuclear density profiles.

The rest of this paper is organized as follows. In Sec. II, we discuss the inclusive lepton-jet correlation. In Sec. II A, we derive the azimuthal angle dependent lepton-jet correlation in the small-$x$ framework. Then, in Sec. II B, we obtain the harmonics and their analytical expression through the saddle point approximation. The QED correction to the harmonics is discussed in Sec. II C. Comprehensive numerical calculations of the inclusive lepton-jet harmonics are presented in Sec. II D. In Sec. III, we explore the diffractive lepton-jet correlation. In Sec. III A, we demonstrate that the rapidity of the diffractive lepton-jet production is the same as in the semi-inclusive diffractive DIS process. The numerical calculations for the harmonics are presented in Sec. II D.

## II. LEPTON-JET CORRELATION

In deeply inelastic scattering, an energetic lepton scatters off a proton or nucleus target,

$$\ell(k) + \mathrm{A}(p) \to \ell'(k_\ell) + \mathrm{Jet}(k_J) + X. \tag{1}$$

In this process, we detect the scattered lepton and final jet, measuring the azimuthal angle between them. The momentum and rapidity of the outgoing lepton are denoted as $k_\ell$ and $y_\ell$, while the momentum and rapidity of the final jet are $k_J$ and $y_J$.

At leading order, the differential cross-section of lepton-jet correlation in the correlation limit can be expressed as

$$\frac{d^5\sigma^{(0)}}{dy_l d^2P_\perp d^2q_\perp} = \sigma_0 \int d^2v_\perp \delta^{(2)}(q_\perp - v_\perp) x f_q(x, v_\perp), \quad (2)$$

where $\sigma_0 = (\alpha_e^2/\hat{s}Q^2)[2(\hat{s}^2+\hat{u}^2)/Q^4]$ with $\hat{s}$, $\hat{u}$ as Mandelstam variables of the partonic subprocess and $Q^2 = -(k-k_\ell)^2$ as the virtuality of the photon. The variable $x$ represents the longitudinal momentum fraction of the incoming quark with respect to the target proton or nucleus. At this order and considering the small initial quark transverse momentum $v_\perp$, the rapidities of the two final particles are correlated due to the constraints $1 = \frac{k_{\ell\perp}}{\sqrt{s_{eN}}}(e^{y_\ell} + e^{y_J})$ and $x = \frac{k_{\ell\perp}}{\sqrt{s_{eN}}}(e^{-y_\ell} + e^{-y_J})$, where $\sqrt{s_{eN}}$ is the center-of-mass energy of the incoming lepton and nucleon. Considering the above constraints relating $y_l, y_J, k_{\ell\perp}(P_\perp), \sqrt{s_{eN}}$, $\sigma_0$ can be rewritten as $\sigma_0 = 2\alpha_e^2 e^{2y_l}(P_\perp^2 e^{2y_l} + s_{eN})/[P_\perp^2 s_{eN}^2 - P_\perp^3 s_{eN}^{3/2} e^{y_l}]$. The $f_q(x, v_\perp)$ is the unintegrated quark distribution in the small-$x$ framework, its expression in coordinate space [123,166–169] after the Fourier transform reads

$$\begin{aligned} x f_q(x, b_\perp) = &\frac{N_c S_\perp}{8\pi^4} \int d\epsilon_f^2 d^2r_\perp \frac{(\vec{b}_\perp + \vec{r}_\perp)\cdot\vec{r}_\perp}{|\vec{b}_\perp + \vec{r}_\perp||\vec{r}_\perp|} \\ &\times \epsilon_f^2 K_1(\epsilon_f|\vec{b}_\perp + \vec{r}_\perp|) K_1(\epsilon_f|\vec{r}_\perp|) \\ &\times [1 + \mathcal{S}_x(b_\perp) - \mathcal{S}_x(b_\perp + r_\perp) - \mathcal{S}_x(r_\perp)]. \quad (3) \end{aligned}$$

In this expression, $S_\perp$ represents the averaged transverse area of the target hadron, while $\mathcal{S}_x(r_\perp)$ denotes the dipole scattering matrix with $r_\perp$ as the transverse size of the dipole. The $\epsilon_f^2 = z(1-z)Q^2$ involves the momentum fraction $z$ for quark/antiquark in the dipole. In the CGC effective theory, the distribution of the initial quark transverse momentum $\vec{v}_\perp$ is isotropic, resulting in the leading order lepton-jet correlation Eq. (2) being independent of the azimuthal angle.

### A. Azimuthal angle dependent lepton-jet correlation

#### 1. One soft gluon radiation

Soft gluon radiations from the final jet introduce azimuthal angle dependence. The azimuthal angle $\phi$ is defined as the angle between the imbalanced momentum $\vec{q}_\perp$ and the relative momentum $\vec{P}_\perp$. We start from one soft gluon radiation.

At one-loop order, one additional soft gluon radiation introduces the azimuthal angle dependence,

$$\begin{aligned} \frac{d^5\sigma^{(1)}}{dy_l d^2P_\perp d^2q_\perp} = &\sigma_0 \int d^2v_\perp x f_q(x, v_\perp) \\ &\times \int d^2k_{g\perp} S(k_{g\perp}) \delta^{(2)}(q_\perp + k_{g\perp} - v_\perp), \quad (4) \end{aligned}$$

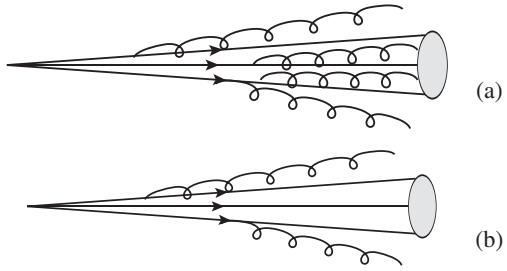


FIG. 2. (a) Soft gluon radiation from the final jet before subtraction. (b) Soft gluon radiation from the final jet after subtracting contributions inside the jet cone.

where $S(k_{g\perp})$ is the eikonal formula, representing the probability of one gluon radiation from the initial quark and the final jet,

$$S(k_{g\perp}) = g^2 C_F \int \frac{dy_g}{2(2\pi)^3} \frac{2k_J \cdot k_q}{k_J \cdot k_g k_q \cdot k_g}. \quad (5)$$

Here, $k_q$ and $k_J$ refer to the momenta of the incoming quark and final jet, respectively. In the calculation of the eikonal formula, it is necessary to subtract the contribution from the soft gluon inside the jet cone by imposing the constraint,

$$\Delta_{k_g k_J} = (y_g - y_J) + (\phi_g - \phi_J)^2 > R^2. \quad (6)$$

The variables $y_g$, $y_J$ and $\phi_g, \phi_J$ represent the rapidities and azimuthal angles of the gluon and jet, respectively. The relative angle between one soft gluon and the jet, denoted as $\phi_g - \phi_J$, is the azimuthal angle $\phi$ under the correlation limit. Figure 2 demonstrates the subtraction of soft gluons inside the jet cone. After the subtraction, the eikonal formula $S(k_{g\perp})$ is given by

$$\begin{aligned} S(k_{g\perp}) = &\frac{g^2 C_F}{(2\pi)^3} \frac{1}{k_{g\perp}^2} \left\{ \ln \frac{Q^4}{k_{g\perp}^2 k_{J\perp}^2} + \frac{2\cos\phi}{\sin\phi}(\pi - \phi) - 2y_+ \right. \\ &- \frac{2\cos\phi}{\sin\phi} \left[ \tan^{-1}\left( \frac{e^{y_+} - \cos\phi}{\sin\phi} \right) \right. \\ &\left. \left. - \tan^{-1}\left( \frac{e^{y_-} - \cos\phi}{\sin\phi} \right) \right] \right\}, \quad (7) \end{aligned}$$

where $y_\pm = \pm\sqrt{R^2 - \phi^2}$. By performing harmonic analysis with respect to the azimuthal angle, the eikonal formula can be expressed as $S(k_{g\perp}) = S_{\rm iso}(k_{g\perp}) + S_{\rm aniso}(k_{g\perp})$. The isotropic and anisotropic components are given by

$$\begin{aligned} S_{\rm iso}(k_{g\perp}) &= \frac{\alpha_s C_F}{2\pi^2 k_{g\perp}^2} \left[ \ln \frac{Q^2}{k_{g\perp}^2} + \ln \frac{Q^2}{k_{J\perp}^2} + c_0(R) \right], \\ S_{\rm aniso}(k_{g\perp}) &= \frac{\alpha_s C_F}{2\pi^2 k_{g\perp}^2} 2 \sum_{n=1}^{\infty} c_n(R) \cos n\phi. \quad (8) \end{aligned}$$

The harmonic coefficients of the final jet cone $R$ can be evaluated using the following formula:

$$c_n(R) = \frac{2}{\pi}\int_0^R d\phi \left\{ \frac{\cos\phi}{\sin\phi}\left[(\pi-\phi) - \tan^{-1}\left(\frac{e^{y_+}-\cos\phi}{\sin\phi}\right) + \tan^{-1}\left(\frac{e^{y_-}-\cos\phi}{\sin\phi}\right)\right] - y_+ \right\} \cos n\phi + \frac{2}{\pi}\int_R^\pi d\phi \frac{\cos\phi}{\sin\phi}(\pi-\phi)\cos n\phi. \tag{9}$$

The two integration regions come from the constraint $\phi \le R$ for some terms of Eq. (7) containing $y_\pm$. These equations are general expressions for both large and small $R$. For a small jet cone with $R \ll 1$, the simplified expressions of $S_{\rm iso}(k_{g\perp})$ and $c_n(R)$ can be found in the paper by Hatta *et al.* [121].

In this one-loop oder calculation, we assume the validity of small-$x$ factorization for the back-to-back lepton-jet production. A more rigorous demonstration of the small-$x$ factorization of the lepton-jet correlation would involve subtracting the rapidity divergences and ensuring the cancellation of infrared divergences, as demonstrated in previous studies [25,26,29,170,171]. The subtracted rapidity divergence from real and virtual diagrams is then renormalized into the small-$x$ parton distribution [169–171], following the procedures in Refs. [18,60]. The infrared divergences cancel between real and virtual diagrams, leaving finite term that include Sudakov type logarithms.

The delta function in Eq. (4) facilitates the Fourier transform of the cross section to the $b_\perp$ space,

$$\frac{d^5\sigma^{(1)}}{dy_l d^2P_\perp d^2q_\perp} = \sigma_0 \int \frac{d^2b_\perp}{(2\pi)^2} e^{i\vec{q}_\perp\cdot\vec{b}_\perp} x f_q(x,b_\perp) \times [S_{\rm iso}(b_\perp) + S_{\rm aniso}(b_\perp)]. \tag{10}$$

When fourier transforming to $b_\perp$-space, the isotropic part has the corresponding virtual diagram contribution that cancels the infrared divergences. Afterwards, we still encounter single and double logarithms in terms of $Q^2/\mu_b^2$, as follows:

$$S_{\rm iso}(b_\perp) = -\int_{\mu_b}^{Q}\frac{d\mu}{\mu}\frac{\alpha_s(\mu)C_F}{\pi}\left[\ln\frac{Q^2}{\mu^2} + \ln\frac{Q^2}{P_\perp^2} + c_0(R)\right], \tag{11}$$

where $\mu_b = b_0/b_\perp$ with $b_0 \equiv 2e^{-\gamma_E}$ and $\gamma_E$ as the Euler constant.

The anisotropic part is convergent, as can be seen in $b_\perp$ space via the Fourier transform. By utilizing the Jacobi-Anger expansion formula,

$$e^{iz\cos(\phi)} = J_0(z) + 2\sum_{n=1}^{\infty} i^n J_n(z)\cos(n\phi), \tag{12}$$

and the integration formula for the Bessel function,

$$\int_0^\infty \frac{dz}{z} J_n(z|b_\perp|) = \frac{1}{n}, \tag{13}$$

we obtain the expression for the anisotropic part in $b_\perp$ space,

$$S_{\rm aniso}(b_\perp) = \frac{\alpha_s C_F}{\pi}\sum_n i^n c_n \frac{2\cos n\phi_b}{n}, \tag{14}$$

where $\phi_b$ represents the angle between $b_\perp$ and $k_{J\perp}$.

#### 2. Multiple soft gluon resummation

When considering contributions from soft gluon emissions to all orders, the isotropic part has been resummed into the exponential factor,

$$\frac{d^5\sigma}{dy_l d^2P_\perp d^2q_\perp} \approx \sigma_0 \int \frac{d^2b_\perp}{(2\pi)^2} e^{i\vec{q}_\perp\cdot\vec{b}_\perp} x f_q(x,b_\perp) \times e^{S_{\rm iso}(b_\perp)}[1 + S_{\rm aniso}(b_\perp)]. \tag{15}$$

The isotropic part corresponds to the Sudakov factor, denoted as $S_{\rm iso}(b_\perp) = -{\rm Sud}(b_\perp)$. Techniques for Sudakov resummation are developed in Refs. [18,60] and [121,122,126,127]. Compared to the Sudakov factor in the collinear factorization framework [121], there is a difference of a single logarithmic term with the coefficient $-3/2$. In the TMD framework, this term arises from the collinear divergence. However, in the small-$x$ framework being considered here, this term is absent.

By using Eq. (12) and integrating over $\phi_b$, we obtain the azimuthal angle dependent lepton-jet correlation,

$$\frac{d^5\sigma(\ell P \to \ell' J)}{dy_\ell d^2P_\perp d^2q_\perp} = \sigma_0 \int \frac{b_\perp db_\perp}{2\pi} x f_q(x,b_\perp) e^{-{\rm Sud}(b_\perp)} \times \left[J_0(q_\perp b_\perp) + \sum_{n=1}^{\infty} 2\cos(n\phi) \times \frac{\alpha_s(\mu_b)C_F c_n(R)}{n\pi} J_n(q_\perp b_\perp)\right]. \tag{16}$$

In the calculation, it is important to note that the angle between $b_\perp$ and $P_\perp$ is set to $(\pi - \phi_b)$. Consequently, the phase factor $e^{i\vec{q}_\perp\cdot\vec{b}_\perp}$ can be expressed as $e^{iq_\perp b_\perp\cos[\phi-(\pi-\phi_b)]}$.

### B. Harmonics and its analytical expression

To quantify the azimuthal anisotropy of the lepton-jet correlation, we define the harmonics or Fourier coefficient of the azimuthal angle dependent lepton-jet correlation as

$$\langle \cos n\phi \rangle = \frac{\sigma_0 \int b_\perp db_\perp J_n(q_\perp b_\perp) W(x, b_\perp) \frac{\alpha_s(\mu_b) C_F c_n(R)}{n\pi}}{\sigma_0 \int b_\perp db_\perp J_0(q_\perp b_\perp) W(x, b_\perp)}. \tag{17}$$

$W$ function is defined as

$$W(x, b_\perp) = x f_q(x, b_\perp) e^{-\mathrm{Sud}(b_\perp)}. \tag{18}$$

In the small $q_\perp$ limit, we can expand the Bessel function by

$$J_n(q_\perp b_\perp) \sim (q_\perp b_\perp/2)^n / \Gamma(n+1). \tag{19}$$

The $n$th harmonic is proportional to $q_\perp^n$, $\langle \cos n\phi \rangle \sim \mathcal{C}_n q_\perp^n$. We now elaborate on how to get an analytical expression for the power-law coefficient $\mathcal{C}_n$.

The Sudakov factor contains the large logarithm $\ln Q^2$ under the correlation limit $Q \geq P_\perp \gg q_\perp$, which serves as a large parameter for the saddle point approximation [172–175]. We evaluate the two integrals in the numerator and denominator using this formula,

$$\int_{-\infty}^{+\infty} dz F(z) e^{-E(z)} \approx \left[\frac{2\pi}{E''(z^{\mathrm{sp}})}\right]^{1/2} F(z^{\mathrm{sp}}) e^{-E(z^{\mathrm{sp}})}, \tag{20}$$

where $z = \ln(\Lambda_{\mathrm{QCD}} b_\perp)$. The saddle point can be determined by

$$\left.\frac{dE(z)}{dz}\right|_{z=z_{\mathrm{sp}}} = 0 \quad \text{with} \quad E''(z) > 0. \tag{21}$$

The harmonics are

$$\langle \cos n\phi \rangle \approx \left(\frac{q_\perp b_0}{2\Lambda_{\mathrm{QCD}}}\right)^n \frac{\alpha_s(\mu_n^{\mathrm{sp}}) C_F c_n(R)}{\pi n \Gamma(n+1)} \frac{f_q(x, b_{\perp n}^{\mathrm{sp}})}{f_q(x, b_{\perp 0}^{\mathrm{sp}})} \times \left[\frac{2\beta_1 + C_F}{(n+2)\beta_1 + C_F}\right]^{1 + \frac{C_F}{2\beta_1} \ln \frac{e^{c_0(R)} Q^4}{\Lambda_{\mathrm{QCD}}^2 P_\perp^2}}, \tag{22}$$

where $\beta_1 = (33 - 2n_f)/12$, $\mu_n^{\mathrm{sp}} = b_0/b_{\perp n}^{\mathrm{sp}}$, $b_0 \equiv 2e^{-\gamma_E}$. The saddle points $b_{\perp n}^{\mathrm{sp}}$ are

$$b_{\perp n}^{\mathrm{sp}} = \frac{b_0}{\Lambda_{\mathrm{QCD}}} \left[\frac{e^{c_0(R)} Q^4}{\Lambda_{\mathrm{QCD}}^2 P_\perp^2}\right]^{-\frac{C_F}{2(2+n)\beta_1 + 2C_F}}. \tag{23}$$

The saddle point approximation is a widely used technique in high energy physics. In particular, the saddle point with $n = 0$ in this context is similar to the saddle point discussed in Ref. [174]. The typical values of the saddle points for the lepton-jet correlation are estimated to be around 1.5 $\mathrm{GeV}^{-1}$ for $b_{\perp 0}^{\mathrm{sp}}$ and roughly 2.5 $\mathrm{GeV}^{-1}$ for the cases, where $n$ equals 1, 2, or 3 for EIC kinematics.

From the analytical expression of the harmonics given in Eq. (22), we know the information about the parton saturation is encoded in the ratio of unintegrated quark distribution $f_q(x, b_\perp^{\mathrm{sp}})$. It is observed that as $Q \geq P_\perp \to \infty$, the saddle points $b_{\perp n}^{\mathrm{sp}}$ approach zero. Hence, we can employ small-$b_\perp$ approximation of $f_q(x, b_\perp^{\mathrm{sp}})$ as follows:

$$f_q(x, b_\perp^{\mathrm{sp}}) \propto Q_s^2 \ln \frac{1}{Q_s b_\perp^{\mathrm{sp}}}, \tag{24}$$

as explained in [168,169]. Thus, the harmonics have the following asymptotic form:

$$\langle \cos n\phi \rangle \propto \frac{f_q(x, b_{\perp n}^{\mathrm{sp}})}{f_q(x, b_{\perp 0}^{\mathrm{sp}})} \approx \frac{\ln(Q_s b_{\perp n}^{\mathrm{sp}})}{\ln(Q_s b_{\perp 0}^{\mathrm{sp}})}. \tag{25}$$

The derivative of $\langle \cos n\phi \rangle$ with respect to $Q_s$ reads

$$\frac{\partial \langle \cos n\phi \rangle}{\partial Q_s} = \frac{\ln b_{\perp 0}^{\mathrm{sp}}/b_{\perp n}^{\mathrm{sp}}}{Q_s \ln^2(Q_s b_{\perp 0}^{\mathrm{sp}})}. \tag{26}$$

Since $b_{\perp n}^{\mathrm{sp}} > b_{\perp 0}^{\mathrm{sp}}$ according to Eq. (23), the derivative is negative. As the saturation momentum $Q_s$ increases, the harmonics decrease. We can observe this feature in the numerical calculations.

### C. QED radiation contribution to the harmonics

Soft gluon radiations can occur in the QCD sector of lepton-jet scattering, while soft photon radiations can occur in the QED sector [121,176,177]. Moreover, soft photon emissions from the final state lepton also contribute to the azimuthal anisotropy [1,121], as depicted in Fig. 1.

Soft photons tend to align with the final lepton, which is the away side of final jet direction. This alignment may reduce the odd harmonics and increase the even harmonics, since $\cos n\phi$ with even $n$ exhibits a symmetric shape, while $\cos n\phi$ with odd $n$ shows an asymmetric shape between 0 and $\pi$ in the azimuthal angle.

By calculating the similar eikonal formula,

$$S_\gamma(k_{g\perp}) = e^2 \int \frac{dy_\gamma}{2(2\pi)^3} \frac{2k_J \cdot k_q}{k_J \cdot k_\gamma k_q \cdot k_\gamma}, \tag{27}$$

we obtain the isotropic and anisotropic part of the eikonal formula for one photon radiation,

$$S_{\mathrm{iso}}^\gamma(b_\perp) = -\int_{\mu_b}^{Q} \frac{d\mu}{\mu} \frac{\alpha_e}{\pi} \left[\ln \frac{Q^2}{\mu^2} + \ln \frac{Q^2}{P_\perp^2} - \frac{3}{2} + c_0^\gamma\right],$$
$$S_{\mathrm{aniso}}^\gamma(b_\perp) = \frac{\alpha_e}{\pi} \sum_n i^n c_n^\gamma \frac{2\cos n\phi_b}{n}, \tag{28}$$

with

$$c_n^\gamma = (-1)^n \left[ \ln \frac{P_\perp^2}{m_e^2} + \frac{2}{\pi} \int_0^\pi d\phi (\pi - \phi) \frac{\cos\phi}{\sin\phi} (\cos n\phi - 1) \right], \tag{29}$$

where $m_e$ denotes the electron mass, and $\alpha_e$ represents the QED coupling. When considering multiple soft photon radiations, the isotropic part can be resummed into the QED Sudakov factor $\mathrm{Sud}^\gamma(b_\perp) = -S_{\mathrm{iso}}^\gamma(b_\perp)$. Although there are large logarithms of $P_\perp^2/m_e^2$ present in the anisotropic part, we only retain the leading order contribution from the anisotropic part, as the small QED coupling constant $\alpha_e \approx 1/137$ compensates for the large logarithms. The harmonics with QED correction reads

$$\langle \cos n\phi \rangle_{\mathrm{QED}} = \frac{\sigma_0 \int b_\perp db_\perp J_n(q_\perp b_\perp) W_{\mathrm{QED}}(x, b_\perp) \frac{[\alpha_s(\mu_b) C_F c_n(R) + \alpha_e c_n^\gamma]}{n\pi}}{\sigma_0 \int b_\perp db_\perp J_0(q_\perp b_\perp) W_{\mathrm{QED}}(x, b_\perp)}, \tag{30}$$

with

$$W_{\mathrm{QED}}(x, b_\perp) = x f_q(x, b_\perp) e^{-\mathrm{Sud}(b_\perp) - \mathrm{Sud}^\gamma(b_\perp)}. \tag{31}$$

The QED Sudakov factor is negligible compared to the QCD Sudakov factor, due to the smallness of the QED coupling constant $\alpha_e$. However, the QED correction to the coefficient $\alpha_s C_F c_n + \alpha_e c_n^\gamma$ is sizable. The numerical calculations in the next section will illustrate these two features.

### D. Numerical calculation of the harmonics

The first calculation involves computing the harmonics for both nonsaturation and saturation models, considering both proton and nucleus target.

The harmonics of the nonsaturation model can be calculated using the same formula as Eq. (17), but with a different $\tilde{W}$ function,

$$\tilde{W} = \sum_q e_q^2 x f_q(x, \mu_b) e^{-\widetilde{\mathrm{Sud}}(b_\perp)}. \tag{32}$$

The $f_q(x, \mu_b)$ represents the collinear quark distribution, encompassing both valence and sea quarks. For the proton, we utilize the NLO PDF sets of CT18A [178], while for the gold nucleus, we adopt the EPPS21 [179] PDF sets. Compared with the Sudakov factor of the saturation model in Eq. (11), the Sudakov factor,

$$\widetilde{\mathrm{Sud}}(b_\perp) = \int_{\mu_b}^{Q} \frac{d\mu}{\mu} \frac{\alpha_s(\mu) C_F}{\pi} \left[ \ln \frac{Q^2}{\mu^2} + \ln \frac{Q^2}{P_\perp^2} - \frac{3}{2} + c_0(R) \right], \tag{33}$$

has an extra $-3/2$ term, corresponding to the collinear divergence [121]. In the numerical calculation, we introduce the nonperturbative Sudakov factor [180,181],

$$\widetilde{\mathrm{Sud}}(b_\perp) \to \widetilde{\mathrm{Sud}}(b_*) + \widetilde{\mathrm{Sud}}_{\mathrm{NP}}^q(b_\perp), \tag{34}$$

with $b_*$-prescription $b_\perp^* = b_\perp/\sqrt{1 + b_\perp^2/b_{\max}^2}$, and $b_{\max} = 1.5\ \mathrm{GeV}^{-1}$. Here, we only include the nonperturbative Sudakov factor associated with the initial quark $\widetilde{\mathrm{Sud}}_{\mathrm{NP}}^q(b_\perp)$, ignoring that of the final jet $\widetilde{\mathrm{Sud}}_{\mathrm{NP}}^{\mathrm{jet}}(b_\perp)$ [121]. This choice allows for a direct comparison with the saturation model.

For the saturation model, we consider two parametrizations for the dipole scattering matrix $\mathcal{S}_x(r_\perp)$ in the unintegrated quark distribution $f_q(x, v_\perp)$ as given in Eq. (3). The first one is the GBW model [182],

$$\mathcal{S}_x(r_\perp) = e^{-\frac{r_\perp^2 Q_s^2(x)}{4}}, \tag{35}$$

where the saturation momentum squared for proton is $Q_{s,p}^2(x) = (x_0/x)^{0.28}\ \mathrm{GeV}^2$ with $x_0 = 3 \times 10^{-4}$. The saturation momentum squared of the gold nucleus is approximately $Q_{s,A}^2 \approx 5 Q_{s,p}^2$. The other parametrization for the dipole scattering matrix is the solution of the running-coupling Balitsky-Kovchegov (rcBK) equation [183–193], with the modified McLerran-Venugopalan (MV) [187,194] model as the initial condition,

$$\mathcal{S}_{x_0}(r_\perp) = e^{-\frac{(r_\perp^2 Q_{s0}^2)^\gamma}{4} \ln\left(\frac{1}{\Lambda r_\perp} + e\right)}, \tag{36}$$

with $\gamma = 1.118$, $\Lambda = 0.241\ \mathrm{GeV}$, and $Q_{s0,p}^2 = 0.16\ \mathrm{GeV}^2$ at $x_0 = 0.01$. For $e + \mathrm{Au}$ rcBK calculation, we solve the rcBK equation with $Q_{s,A}^2 \approx 5 Q_{s,p}^2$. More realistic initial conditions for a dipole-nucleus amplitude [195] can be chosen.

Since the nonperturbative region is usually dominated by the small-x dipole distribution, we do not need to introduce the nonperturbative Sudakov factor for the saturation model. Thus, we simply write

$$\mathrm{Sud}(b_\perp) \to \mathrm{Sud}(b_*), \tag{37}$$

which limits the perturbative Sudakov factor in the small $b_\perp$ region.

The kinematics bins for the future EIC that we use to calculate the $q_\perp$ distribution of $\langle \cos n\phi \rangle$ are $\sqrt{s_{eN}} = 89\ \mathrm{GeV}$, $y_\ell = 2.41$, $0.008 \le x \le 0.01$, $4\ \mathrm{GeV} \le P_\perp \le 4.4\ \mathrm{GeV}$, $5.6\ \mathrm{GeV} \le Q \le 5.9\ \mathrm{GeV}$. The choice of the kinematic region aligns with the simulation study [120] of the EIC. The lower cut for $x$ is determined by given $s_{eN}, P_\perp$, specifically $x_{\min} \approx 4P_\perp^2/s_{\mathrm{eN}}$. The limited collision energy $s_{\mathrm{eN}}$ makes it difficult to probe lower $x$ value ($x \le 1 \times 10^{-3}$) in the lepton-jet correlation.

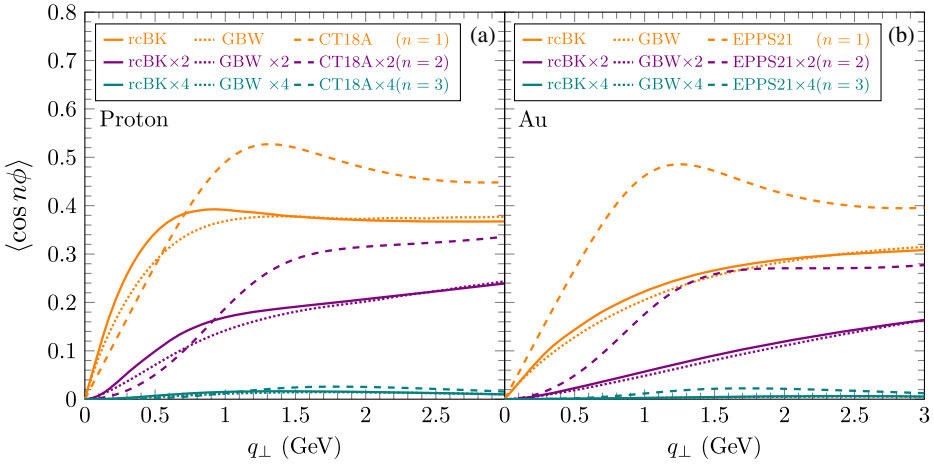


FIG. 3. (a) First three harmonics of inclusive lepton-jet production in $e+p$ collisions using inputs from the rcBK solution, GBW model, and CT18A PDFs. (b) First three harmonics of inclusive lepton-jet production predicted for $e+\mathrm{Au}$ collisions using inputs: the rcBK solution, GBW model, and EPPS21 PDFs. The calculation is for EIC kinematics: $\sqrt{s_{eN}}=89$ GeV, $0.008<x<0.01$, $y_\ell=2.41$ with a jet cone size $R=0.4$. The QED corrections are included.

Figure 3 presents the $q_\perp$ distribution of $\langle\cos n\phi\rangle$ for different models, considering both proton and nucleus targets with a jet cone size $R=0.4$. The results exhibit a common trend: all lines sharply rise from zero in the small-$q_\perp$ region and gradually approach a plateau in the large-$q_\perp$ region. Notably, our results appear to be more flat in the large-$q_\perp$ region compared to the lines shown in Fig. 4 of [121]. The discrepancy arises because our calculation is performed within the 4 GeV $\le P_\perp \le$ 4.4 GeV bin, while their calculation is specific to a single $P_\perp$ value. Besides the common trend, we also observe a hierarchy of harmonics with the harmonic number $n$. Furthermore, the harmonics of the saturation model show a significant decrease from the proton to the gold nucleus target. First, Eq. (26) shows $\partial\langle\cos n\phi\rangle/\partial Q_s<0$, indicating that the harmonics decreases with an increase in $Q_s$. Additionally, the saturation scale squared $Q_{s,A}^2\propto A^{1/3}Q_{s,p}^2$ is larger in the gold nucleus than in the proton. Therefore, we can explain the observed decrease in harmonics from proton to Au in Fig. 3. The results in Fig. 3 include the QED correction, different from similar plots in our previous paper [1].

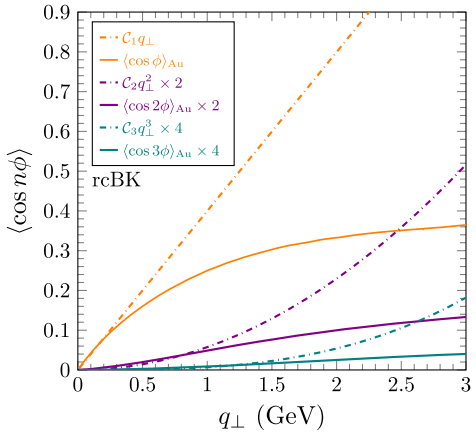


FIG. 4. Comparison of the exact results of harmonics and their small-$q_\perp$ asymptotic behaviors. Solid lines stand for the exact results, while dash-dotted lines depict the small-$q_\perp$ asymptotic expansions given by Eq. (22). The EIC kinematics for calculation are $\sqrt{s_{eN}}=89$ GeV, $x=0.008$, $y_\ell=2.41$ with a jet cone size $R=0.4$. The QED corrections are not included.

In Fig. 4, the analytical expression of harmonics for small-$q_\perp$ given by Eq. (22) from Sec. II B is plotted and compared it with harmonics obtained for the rcBK model with a gold nucleus target. The harmonics are calculated for the specific value of $x=0.008$. The comparison validates the analytical expression of harmonics at small $q_\perp$.

To further quantify the suppression of the anisotropy in $e+\mathrm{Au}$ collisions compared to $e+p$ collisions, we define the nuclear modification factor as follows:

$$R_{eA}^{(n)}=\frac{\langle\cos n\phi\rangle_{eA}}{\langle\cos n\phi\rangle_{ep}}. \tag{38}$$

In Fig. 5, we plot the nuclear modification factor for the nonsaturation model and the saturation model. The nonsaturation model utilizes the EPPS21 gold nucleus PDFs and the CT18A proton PDFs, with the error band at 90% confidence level. We neglect the uncertainties from the baseline proton PDFs, as they are small. On the other hand, the saturation model employs the rcBK solution, where the gold saturation scale squared $Q_{s,A}^2$ varies from $3Q_{s,p}^2$ (upper bound in each band) to $5Q_{s,p}^2$ (lower bound). The $R_{eA}^{(n)}$ predicted from EPPS21 PDFs (nonsaturation model) and the rcBK solution (saturation model) show distinct behaviors in the small-$q_\perp$ region and converge to unity in the large-$q_\perp$ region. This difference justifies the

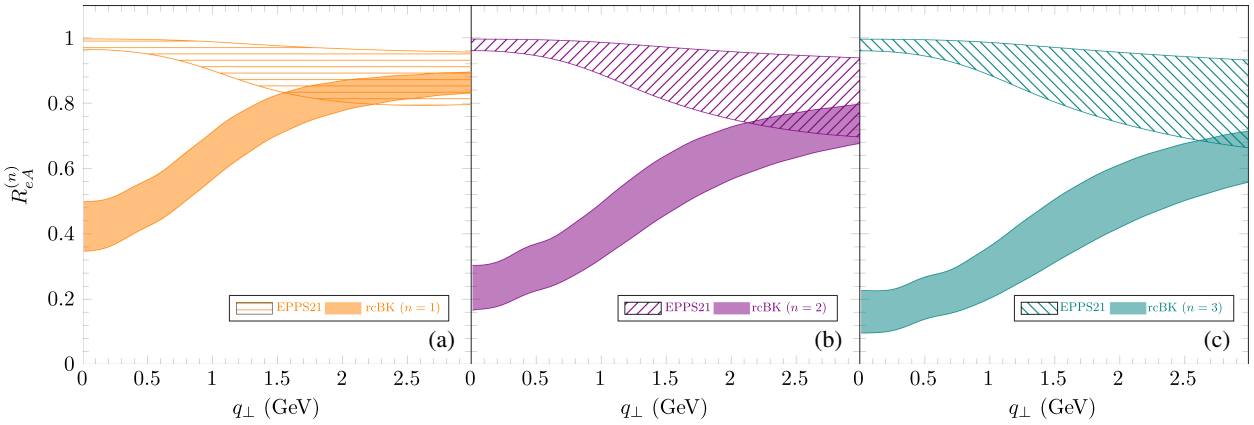


FIG. 5. Nuclear modification factors of the inclusive lepton-jet harmonics for the cases where $n = 1$, 2, and 3. The upper bands represent $R_{eA}^{(n)}$ based on the inputs of the EPPS21 gold nuclear PDFs with uncertainties. The lower bands yield $R_{eA}^{(n)}$ calculated with the rcBK solution, where the gold saturation scale $Q_{s,A}^2$ varies from $3Q_{s,p}^2$ (upper bound in each band) to $5Q_{s,p}^2$ (lower bound). The EIC kinematics for the calculation are $\sqrt{s_{eN}} = 89$ GeV, $0.008 < x < 0.01$, $y_\ell = 2.41$ with a jet cone size $R = 0.4$.

nuclear modification factor as a tool to distinguish between the saturation and nonsaturation frameworks.

In Fig. 5, the hierarchy observed in the nuclear modification factor of the saturation models is explained by the asymptotic expression of the harmonics, Eq. (25). By substituting the $Q_{s,A}^2 \approx 5Q_{s,p}^2$ in Eq. (25), we find

$$R_{eA}^{(n)} \propto \frac{\ln(5Q_{s,p}^2 b_{\perp n}^{\rm sp})}{\ln(Q_{s,p}^2 b_{\perp n}^{\rm sp})} \frac{\ln(Q_{s,p}^2 b_{\perp 0}^{\rm sp})}{\ln(5Q_{s,p}^2 b_{\perp 0}^{\rm sp})}. \tag{39}$$

Given that $b_{\perp n}^{\rm sp}$ increases with $n$, this expression explains the observed decrease in the nuclear modification factor $R_{eA}^{(n)}$ with an increase in $n$ in the numerical results.

Figure 6 shows the harmonics and nuclear modification factor with and without QED correction, using the rcBK solution as the input. The QED corrections for the harmonics are pronounced, leading to a reduction in odd harmonics and an increase in even harmonics. This correction is attributed to the sizable correction in the coefficient $\alpha_s C_F c_n + \alpha_e c_n^\gamma$ in Eq. (30). However, the QED correction to the nuclear modification factor is found to be negligible, as the coefficient $\alpha_s C_F c_n + \alpha_e c_n^\gamma$ cancels between $\langle \cos n\phi \rangle_{eA}$ and $\langle \cos n\phi \rangle_{ep}$. In order to compare with experimental data, all subsequent calculations incorporate QED correction.

Our calculation can be compared with a recent experimental study [196] at HERA, where electron and proton collide at energy of 27.6 GeV and 920 GeV, respectively. The kinematics bin are $0.2 < y < 0.7$, $-1 < \eta_{\rm lab} < 2.5$, $k_{J\perp} > 10$ GeV, $Q^2 > 150$ GeV$^2$. Here, $y = P \cdot q / P \cdot k$ represents the energy fraction taken by the photon from the lepton in lab frame, and $\eta_{\rm lab}$ is the rapidity range that the detector can cover. The jet cone size is $R = 1.0$. In our calculation, we compute the harmonics in this HERA

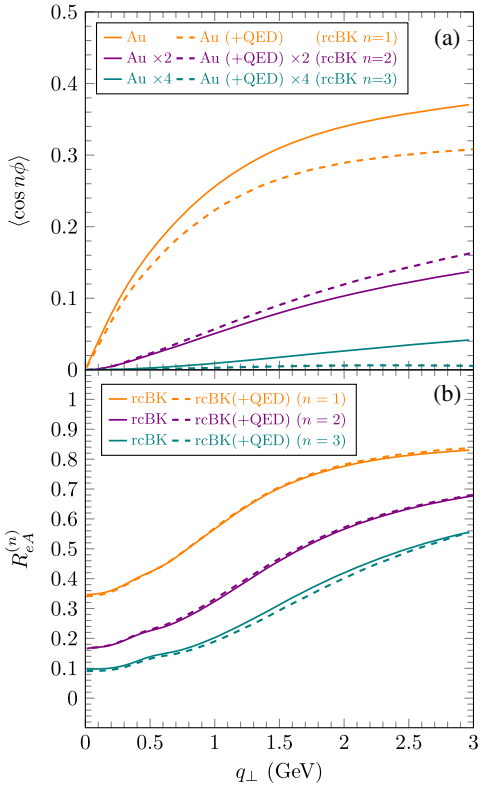


FIG. 6. QED modification to the first three harmonics of the inclusive lepton-jet correlation and nuclear modification factors for $e$ + Au collisions with the input from the rcBK solution. Solid and dashed lines represent the harmonics or nuclear modification factor without and with QED modifications, respectively. The calculation is performed in the following EIC kinematics: $\sqrt{s_{eN}} = 89$ GeV, $0.008 < x < 0.01$,$y_l = 2.41$ with a jet cone size $R = 0.4$.

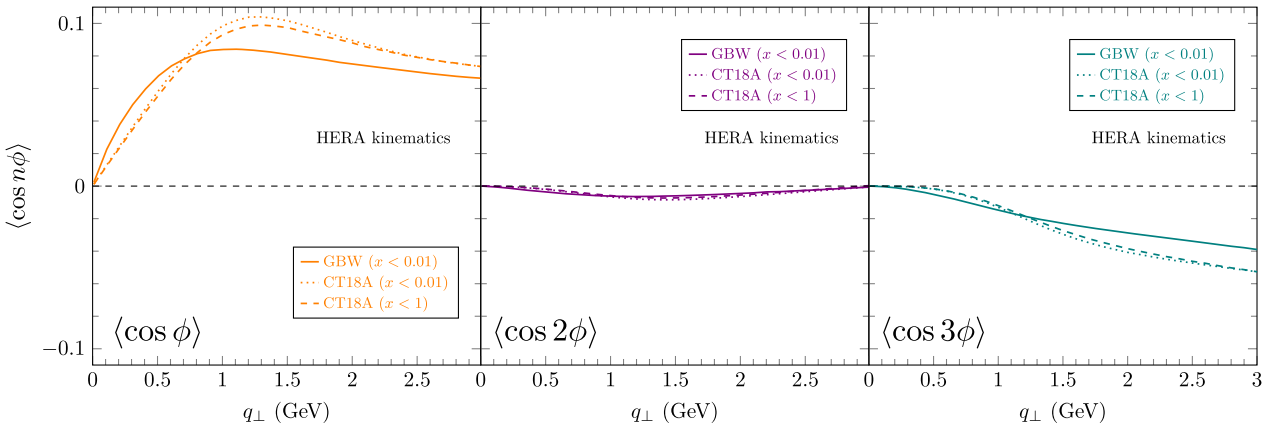


FIG. 7. First three harmonics in $e + p$ collisions with inputs from the GBW model and CT18A PDFs in the HERA kinematics, with additional cut on the initial quark momentum fraction $x$. The HERA kinematics are $0.2 < y < 0.7$, $-1 < \eta_{\rm lab} < 2.5$, $k_{J\perp} > 10$ GeV, $Q^2 > 150$ GeV$^2$ with jet cone $R = 1.0$.

kinematics and present the results in Fig. 7. In the calculation, the kinematic restrictions constrain the rapidity $y_J$ (or $y_l$), $k_{J\perp}$, initial quark momentum fraction $x$ and their combination, since $Q^2, y, \eta_{\rm lab}$ are expressed in terms of $y_J, k_{J\perp}, x$. We compute both saturation framework with the GBW model, and nonsaturation framework with CT18A proton PDFs. For the saturation framework, we apply the extra cut $x < 0.01$, while for the nonsaturation framework, we have two different cuts $x < 0.01$ and $x < 1$. In our calculation, we also include the QED correction.

In Fig. 7, we observe that the harmonics $\cos\phi$ are sizable, while $\langle\cos 2\phi\rangle$ and $\langle\cos 3\phi\rangle$ are almost zero. This behavior can be attributed to the decrease in the Fourier coefficient $c_n(R)$ with increasing $R$, as evident from Fig. 3 in Ref. [121]. The negative values of $\langle\cos 2\phi\rangle$ and $\langle\cos 3\phi\rangle$ also originate from the Fourier coefficient $c_n(R)$ with $R = 1.0$. The observed trend of these harmonics is consistent with the previous results obtained for the EIC kinematics, as shown in Fig. 3.

## III. DIFFRACTIVE LEPTON-JET CORRELATION

In high energy $ep$ and $eA$ collisions, the diffractive lepton-jet process occurs when we observe a large rapidity gap $Y_{\rm IP}$ between the hard interaction part and the remnant proton/nucleus, while also measuring the scattered lepton and one jet, as illustrated in Fig. 8.

The diffractive process can be understood as the proton/nucleus exchanging colorless multiple gluons with the hard interaction part. The momentum transfer in diffraction is denoted as $t = (p' - p)^2 = \Delta^2 \approx -\vec{\Delta}_\perp^2$, while the momentum fraction carried by these colorless gluons from the incoming nucleon is $x_{\rm IP} = n \cdot (p - p')/n \cdot p$, where $n = (0, 1, 0_\perp)$. In Fig. 8, the hard interaction production is denoted as $X$, and its mass is defined as $M$. From the definition of the mass $(x_{\rm IP} p + q)^2 = M^2$, we obtain

$$x_{\rm IP} = \frac{M^2 + Q^2}{W^2 + Q^2}, \tag{40}$$

where $W^2 = (p + q)^2$ represents the center-of-mass energy squared of the photon-nucleon system.

The semi-inclusive diffractive DIS process [128] has been shown to be factorized in terms of the TMD diffractive parton distribution function (DPDF). We assume that diffractive lepton-jet production can also be factorized in terms of the quark TMD DPDF, where the longitudinal momentum fraction carried by quark from colorless multiple gluons is $\beta = x/x_{\rm IP}$. In the small-$x$ framework, the quark TMD DPDF [129,197] is related to the dipole S matrix and encodes information about gluon saturation [128].

The expression of the quark TMD DPDF in $k_\perp$ space is taken from Ref. [128],

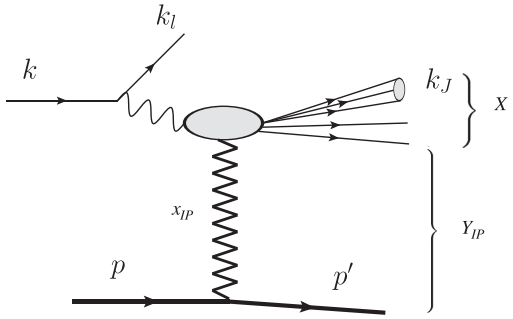


FIG. 8. Diffractive lepton-jet production process in DIS. The final state lepton, along with one final jet, can be measured. The incoming nucleon exchanges multiple gluons in a color singlet state with the virtual photon, having the exchanged longitudinal momentum fraction $x_{\rm IP}$. A large rapidity gap exists between the nucleon remnant $p'$ and the hard interaction production $X$.

$$\frac{df_q^D(\beta,k_\perp,t;x_{\rm IP})}{dY_{\rm IP}dt}=\frac{N_c\beta}{2\pi}\int d^2k_{1\perp}d^2k_{2\perp}\mathcal{F}_{x_{\rm IP}}(k_{1\perp},\Delta_\perp)\times\mathcal{F}_{x_{\rm IP}}(k_{2\perp},\Delta_\perp)\mathcal{T}_q(k_\perp,k_{1\perp},k_{2\perp}),\quad(41)$$

with $\mathcal{T}_q$ defined as sum of four terms $\mathcal{T}_q\equiv T_q(k_\perp,k_{1\perp},k_{2\perp})-T_q(k_\perp,0,k_{2\perp})-T_q(k_\perp,k_{1\perp},0)+T_q(k_\perp,0,0)$, where

$$T_q(k_\perp,k_{1\perp},k_{2\perp})=\frac{(k_\perp-k_{1\perp})\cdot(k_\perp-k_{2\perp})k_\perp^2}{[\beta k_\perp^2+(1-\beta)(k_\perp-k_{1\perp})^2][\beta k_\perp^2+(1-\beta)(k_\perp-k_{2\perp})^2]},\quad(42)$$

and $\mathcal{F}_{x_{\rm IP}}(k_{1\perp},\Delta_\perp)$ represents the Fourier transform of the dipole S matrix in the fundamental representation,

$$\mathcal{F}_{x_{\rm IP}}(k_{1\perp},\Delta_\perp)=\int\frac{d^2b_\perp d^2r_\perp}{(2\pi)^4}e^{i\vec{k}_{1\perp}\cdot\vec{r}_\perp+i\vec{\Delta}_\perp\cdot\vec{b}_\perp}\mathcal{S}_x(r_\perp,b_\perp),\quad(43)$$

where $r_\perp$ is the dipole separation, and $b_\perp$ is the impact parameter.

The azimuthal angle dependent cross-section and harmonics of diffractive process have similar definitions as Eq. (16) and Eq. (17). By replacing the small-$x$ unintegrated quark distribution $f_q(x,b_\perp)$ with small-$x$ quark TMD DPDF, we get the angle dependent diffractive lepton-jet cross section,

$$\frac{d^5\sigma(\ell P\to\ell' J)}{dy_\ell d^2P_\perp d^2q_\perp dY_{\rm IP}dt}=\sigma_0\int\frac{b_\perp db_\perp}{2\pi}W_{\rm diff}\times\left[J_0(q_\perp b_\perp)+\sum_{n=1}^{\infty}2\cos(n\phi)\times\frac{\alpha_s(\mu_b)C_Fc_n(R)}{n\pi}J_n(q_\perp b_\perp)\right],\quad(44)$$

and diffractive harmonics,

$$\langle\cos n\phi\rangle_{\rm diff}=\frac{\sigma_0\int b_\perp db_\perp J_n(q_\perp b_\perp)W_{\rm diff}\frac{\alpha_s(\mu_b)C_Fc_n(R)}{n\pi}}{\sigma_0\int b_\perp db_\perp J_0(q_\perp b_\perp)W_{\rm diff}},\quad(45)$$

where $W_{\rm diff}$ function is defined as

$$W_{\rm diff}(x,\beta,b_\perp;x_{\rm IP})=e^{-{\rm Sud}(b_\perp)}\int d^2k_\perp e^{i\vec{k}_\perp\cdot\vec{b}_\perp}x\frac{df_q^D(\beta,k_\perp,t;x_{\rm IP})}{dY_{\rm IP}dt}.\quad(46)$$

When deriving the diffractive harmonics Eq. (45), we expect that typical events of soft gluon emissions do not contaminate the rapidity gap imposed by the LO diffractive process, e.g., $\gamma^*+A\to{\rm Jet}(q_f)+Z(\bar{q}_f)+A'$. This is because the soft gluon radiations and the resulting harmonics favor the near-jet cone radiations from the hard subprocess $\gamma^*+q_i\to{\rm Jet}(q_f)$ without constrains from the rapidity gap. Here, $q_i$ denotes the initial quark parton struck by the virtual photon $\gamma^*$. As long as the jet cone $R$ is small enough, these soft radiations are expected to be separated from the other subprocess: $A\to q_i+Z(\bar{q}_f)+A'$, which determines the rapidity gap and is described by the diffractive TMD quark PDF.

### A. The rapidity gap in diffractive lepton-jet production

The rapidity gap for semi-inclusive diffractive DIS (SIDDIS) follows the traditional rapidity gap for diffractive process $Y_{\rm IP}\sim\ln 1/x_{\rm IP}$ [198]. SIDDIS is defined in the Breit frame, which is the photon-nucleon center-of-mass frame (frame $C$), while the diffractive lepton-jet process is measured in the lepton-nucleon center-of-mass frame (frame $A$). The rapidity gap of the diffractive lepton jet is different from that of SIDDIS due to the Lorentz transformation between the two frames, which involves a Lorentz rotation.

The frame transformation from the lepton-nucleon center-of-mass frame (frame $A$) to the photon-nucleon center-of-mass frame (frame $C$) can be understood in three steps: (1) The Lorentz boost from frame A to the nucleon rest frame with the lepton moving in the $-z$ direction (frame $B$); (2) The rotation from frame $B$ to the nucleon rest frame with the photon moving in the $-z'$ direction (frame $B'$); (3) The Lorentz boost from frame $B'$ to frame $C$.

The demonstration of the Lorentz rotation [199] can be seen in Fig. 9, with the rotation angle denoted as $\theta$. The rotation angle can be determined from the four-momentum of the virtual photon in these two frame,

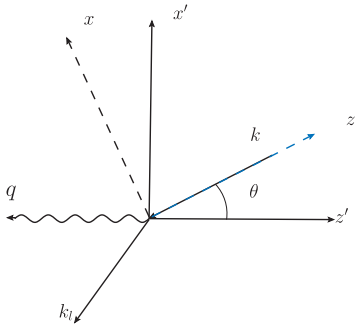


FIG. 9. The rotation from the nucleon rest frame with the lepton moving in the $-z$ direction (frame $B$) to the nucleon rest frame with the photon in the $-z'$ direction (frame $B'$), is depicted in the lepton plane defined by the incoming lepton with momentum $k$ and the outgoing lepton with momentum $k_l$.

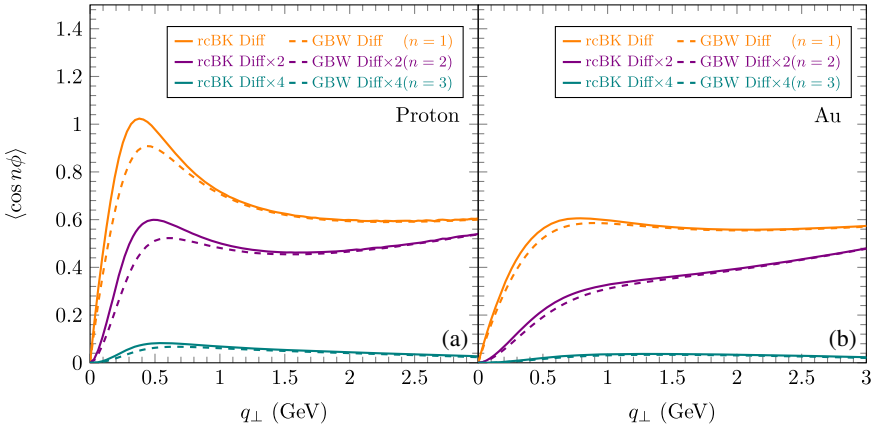


FIG. 10. First three harmonics of diffractive lepton-jet production in (a) $e+p$ collisions and (b) $e+\mathrm{Au}$ collisions with the inputs from the rcBK solution and the GBW model. The EIC kinematics for the calculation are $\sqrt{s_{eN}}=89$ GeV, $\beta=0.94$, $0.008<x<0.0094$, $y_l=2.41$ with a jet cone size $R=0.4$.

$$\tan\theta=-\frac{q_B^1}{q_B^3}, \tag{47}$$

where $q_B=(q_B^0,q_B^1,0,q_B^3)$ is the photon four-momentum in frame $B$. By choosing the kinematics $\sqrt{s_{eN}}=89$ GeV, $y_\ell=y_J=2.41$, $x=0.008$, $P_\perp=4$ GeV, $Q=5.6$ GeV, and $\beta=0.94$, we find that $\theta=0.00187$ for the Lorentz rotation. The Lorentz rotation matrix is nearly an identity matrix, indicating that the rapidity is barely changed by the Lorentz rotation. Since the rapidity gap is invariant under Lorentz boost, the rapidity gap in the photon-nucleon center-of-mass frame (frame $A$) is almost the same value as the rapidity gap in the lepton-nucleon center-of-mass frame (frame $C$). Therefore, we can use $Y_{\mathrm{IP}}\sim\ln 1/x_{\mathrm{IP}}$ to represent the rapidity gap for diffractive lepton-jet production.

### B. Numerical calculation of diffractive harmonics

In the numerical calculation, we first neglect the impact parameter $b_\perp$ dependence of the dipole S matrix and utilize two models for $\mathcal{S}_x(r_\perp)$: the GBW model Eq. (35) and the solution of the rcBK equation with the modified MV model as the initial condition, shown in Eq. (36).

We calculate the $q_\perp$ distribution of the harmonics $\langle\cos n\phi\rangle_{\mathrm{diff}}$. The kinematics bin for diffractive lepton-jet production at the future EIC is defined as follows: $\sqrt{s_{eN}}=89$ GeV, $y_\ell=2.41$, $0.008\le x\le 0.0094$, $\beta=0.94$, $x_{\mathrm{IP}}=x/\beta$, $4\ \mathrm{GeV}\le P_\perp\le 4.32$ GeV, $5.6\ \mathrm{GeV}\le Q\le 5.89$ GeV. The value of $\beta$ can vary, but it should be chosen such that $x_{\mathrm{IP}}$ falls within the range of [0.008, 0.01].

In Fig. 10, we plot the harmonics of diffractive lepton-jet production for saturation models, considering both proton and gold nucleus target, with a jet cone size $R=0.4$. The decrease in harmonics from proton to gold nucleus target is also observed in Fig. 10. Notably, the harmonics of the diffractive process are nearly twice the value of the harmonics of the inclusive lepton-jet process. This behavior can be explained by the asymptotic form of the harmonics, as given in Eq. (25). For the same choice of $Q,P_\perp$ for inclusive and diffractive lepton-jet processes, the saddle point $b_{\perp n}^{\mathrm{sp}}$ values are the same. For example, if $x=0.008$, $P_\perp=4$ GeV, $Q=5.6$ GeV, the saddle points are $b_{\perp 0}^{\mathrm{sp}}=1.68\ \mathrm{GeV}^{-1}$, $b_{\perp 1}^{\mathrm{sp}}=2.22\ \mathrm{GeV}^{-1}$, $b_{\perp 2}^{\mathrm{sp}}=2.59\ \mathrm{GeV}^{-1}$, and $b_{\perp 3}^{\mathrm{sp}}=2.87\ \mathrm{GeV}^{-1}$. We plot the quark TMD DPDF and PDF for $b_\perp\in[0,3]\ \mathrm{GeV}^{-1}$ in Fig. 11. It is evident that in the small $b_\perp$ region, the flat DPDF gives

$$\frac{df_q^D(\beta,b_{\perp n}^{\mathrm{sp}};x_{\mathrm{IP}})}{dY_{\mathrm{IP}}dt}\Big/\frac{df_q^D(\beta,b_{\perp 0}^{\mathrm{sp}};x_{\mathrm{IP}})}{dY_{\mathrm{IP}}dt}\approx 1, \tag{48}$$

while the steeply declining PDF results in

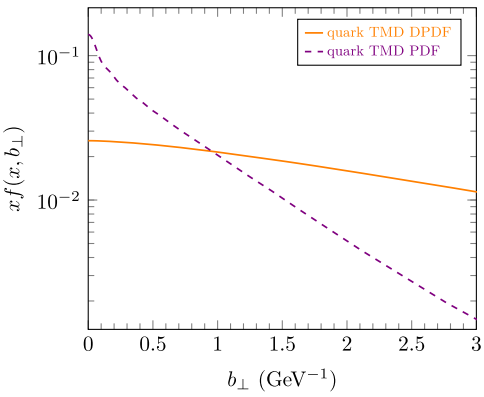


FIG. 11. The comparison between the quark diffractive TMD distribution $x\frac{df_q^D(\beta,b_\perp;x_{\mathrm{IP}})}{dY_{\mathrm{IP}}dt}$ and the quark TMD distribution $xf(x,b_\perp)$ in coordinate space for $b_\perp\in[0,3]\ \mathrm{GeV}^{-1}$.

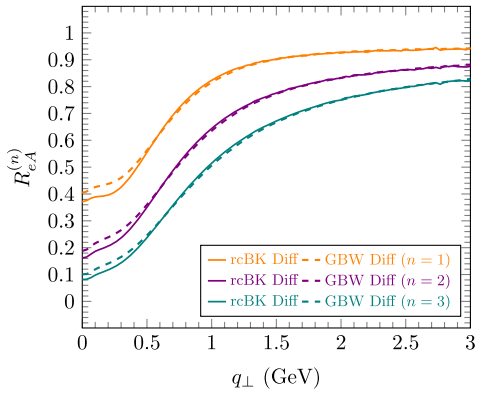


FIG. 12. Nuclear modification factor of the first three harmonics for diffractive lepton-jet production, with the rcBK solution and GBW model as inputs. The EIC kinematics for calculation is $\sqrt{s_{eN}} = 89$ GeV, $\beta = 0.94$, $0.008 < x < 0.0094$, $y_l = 2.41$ with a jet cone size $R = 0.4$.

$$\frac{f(x, b_{\perp n}^{\mathrm{sp}})}{f(x, b_{\perp 0}^{\mathrm{sp}})} \ll 1. \tag{49}$$

This difference causes $\langle \cos n\phi \rangle_{\mathrm{diff}}$ a couple times of $\langle \cos n\phi \rangle$. If we substitute $b_{\perp 0}^{\mathrm{sp}} = 1.68\ \mathrm{GeV}^{-1}$, $b_{\perp 1}^{\mathrm{sp}} = 2.22\ \mathrm{GeV}^{-1}$ into the ratio of DPDF and PDF, we obtain

$$\frac{df_q^D(\beta, b_{\perp 1}^{\mathrm{sp}}; x_{\mathrm{IP}})}{dY_{\mathrm{IP}} dt} \Big/ \frac{df_q^D(\beta, b_{\perp 0}^{\mathrm{sp}}; x_{\mathrm{IP}})}{dY_{\mathrm{IP}} dt} = 0.84$$
$$\frac{f(x, b_{\perp n}^{\mathrm{sp}})}{f(x, b_{\perp 0}^{\mathrm{sp}})} = 0.48. \tag{50}$$

This explains $\langle \cos n\phi \rangle_{\mathrm{diff}} \approx 2\langle \cos n\phi \rangle$.

We also plot the nuclear modification factor for diffractive harmonics in Fig. 12, using both the GBW model and rcBK solution as inputs. Surprisingly, the nuclear modification factor of diffractive lepton-jet harmonics is nearly identical to that of inclusive lepton-jet harmonics in Fig. 5. The larger harmonics and nearly identical nuclear modification factor, compared to inclusive lepton-jet production, make them even better observables for studying saturation phenomenon.

To study the $t$ dependence of the harmonics and explore the sensitivity to nuclear density profiles, we restore the impact factor $b_\perp$ dependence of the quark diffractive PDF. For this analysis, we choose two distinct density profiles for the proton and nucleus: one being a uniform cylinder, the other a uniform sphere.

By considering the proton(nucleus) as a uniform cylinder with radius $r_p(r_A)$, we employ the GBW model for the dipole S matrix. The Fourier transform of the dipole S matrix reads

$$\mathcal{F}_{x_{\mathrm{IP}}}(k_{1\perp}, \Delta_\perp) = \int \frac{d^2 b_\perp d^2 r_\perp}{(2\pi)^4} e^{i\vec{k}_{1\perp}\cdot\vec{r}_\perp + i\vec{\Delta}_\perp\cdot\vec{b}_\perp} e^{-\frac{r_\perp^2 Q_{s,p}^2(x)}{4}}$$
$$= \frac{r_p J_1(r_p \Delta_\perp)}{2\pi\Delta_\perp} \int \frac{d^2 r_\perp}{(2\pi)^2} e^{i\vec{k}_{1\perp}\cdot\vec{r}_\perp} e^{-\frac{r_\perp^2 Q_{s,p}^2(x)}{4}}. \tag{51}$$

In this case, the $t(\Delta_\perp)$ dependence factorizes, leading to its cancellation between the numerator and denominator of the diffractive harmonics in Eq. (45). Consequently, the harmonics of the "cylinderlike" proton do not exhibit $t$ dependence.

For a uniform sphere proton(nucleus), we employ the modified GBW model,

$$\mathcal{S}_x(r_\perp, b_\perp) = e^{-\frac{r_\perp^2 Q_{s,p}^2(x, b_\perp)}{4}}, \tag{52}$$

where

$$Q_{s,p}^2(x, b_\perp) = c_s \sqrt{1 - \frac{b_\perp^2}{r_p^2}}. \tag{53}$$

The radius of the proton is $r_p = 4.2\ \mathrm{GeV}^{-1}$ (for the gold nucleus $r_A = 32.5\ \mathrm{GeV}^{-1}$). To compare with the above cylinder profile, we require that the impact parameter dependent saturation scale squared $Q_{s,p}^2(x, b_\perp)$ satisfies the normalization condition,

$$\int d^2 b_\perp Q_{s,p}^2(x, b_\perp) = \pi r_p^2 Q_{s,p}^2(x). \tag{54}$$

The right-hand side saturation scale squared of the traditional GBW model is given by $Q_{s,p}^2(x) = (x_0/x)^{0.28}\ \mathrm{GeV}^2$ with $x_0 = 3 \times 10^{-4}$. For the gold nucleus, we choose $Q_{s,A}^2(x) = 5Q_{s,p}^2(x)$. As the conjugate variable of $b_\perp$ in the Fourier transform, the $t(\Delta_\perp)$ dependence of diffractive harmonics opens a new dimension to distinguish different nuclear density profiles.

We plot the diffractive harmonics for the cylinder and sphere proton(nucleus) in both HERA and EIC kinematics. Figure 13 displays the results for $e + p$ collisions in the HERA kinematics. For the EIC kinematics, we present predictions for both $e + p$ and $e + \mathrm{Au}$ collisions in Figs. 14 and 15, respectively. For the proton, we compute with $-t = 0.5\ \mathrm{GeV}^2$ and $-t = 1.5\ \mathrm{GeV}^2$. Regarding the gold nucleus, we select $-t = 0.5\ \mathrm{GeV}^2$, $-t = 1.5\ \mathrm{GeV}^2$ and $-t = 5\ \mathrm{GeV}^2$. The sizable difference between the cylinder and sphere proton(nucleus) suggests diffractive harmonics as new probes for the density profile of the target. Various density profiles can be tested in diffractive harmonics in future study, such as Gaussian [43] or a more flexible parametrization [156]. The notable sharp peaks of diffractive harmonics for the sphere shape gold nucleus at $-t = 0.5\ \mathrm{GeV}^2$ in Fig. 15 originate from the diffractive

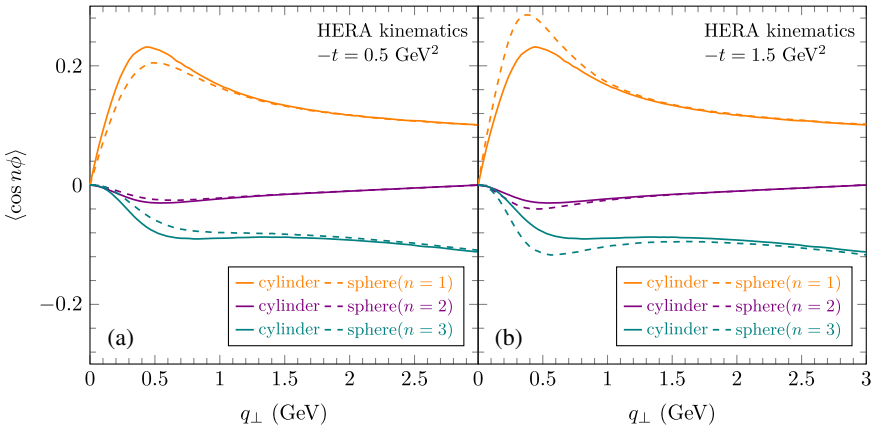


FIG. 13. The comparison of diffractive harmonics in lepton-jet production for $e + p$ collisions in HERA kinematics, considering both cylinder and sphere proton shape. The $t$ has two value (a) $-t = 0.5$ GeV$^2$ and (b) $-t = 1.5$ GeV$^2$. The HERA kinematics include $\sqrt{s_{eN}} = 319$ GeV, $0.2 < y < 0.7$, $-1 < \eta_{\text{lab}} < 2.5$, $k_{J\perp} > 10$ GeV, $Q^2 > 150$ GeV$^2$ with $\beta = 0.94$, $x_{\text{IP}} < 0.01$, $R = 1.0$.

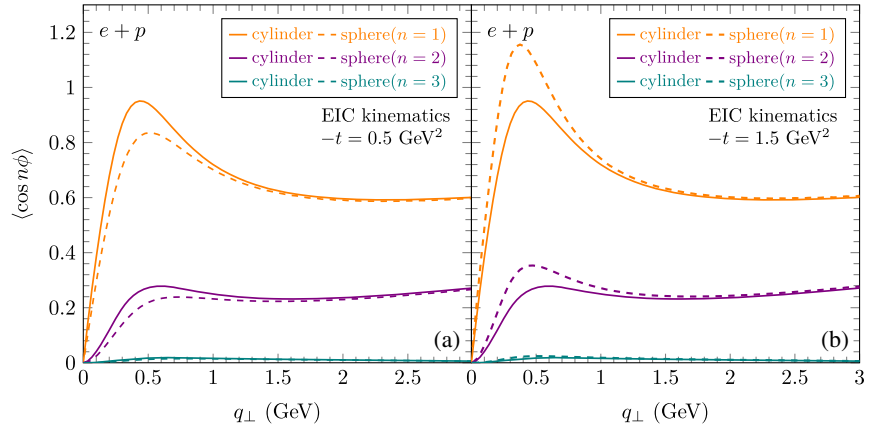


FIG. 14. The comparison of diffractive harmonics of lepton-jet production in $e + p$ collisions in the EIC kinematics, for cylinder and sphere proton shape. The variable $t$ takes two values (a) $-t = 0.5$ GeV$^2$ and (b) $-t = 1.5$ GeV$^2$. The $t$ dependent model assume a sphere shape of the proton. The EIC kinematics are $\sqrt{s_{eN}} = 89$ GeV, $x = 0.008$, $y_l = 2.41$ with $\beta = 0.94$, $x_{\text{IP}} < 0.01$, $R = 0.4$.

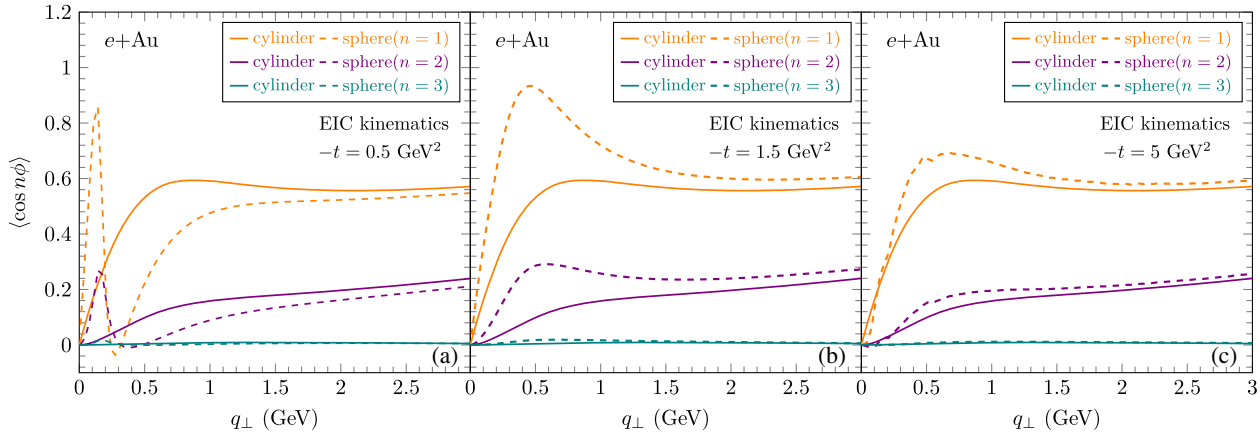


FIG. 15. The comparison of diffractive harmonics of lepton-jet production in $e + \text{Au}$ collisions in the EIC kinematics, for cylinder and sphere gold nucleus shapes. The variable $t$ takes three values (a) $-t = 0.5$ GeV$^2$, (b) $-t = 1.5$ GeV$^2$, and (c) $-t = 5$ GeV$^2$. The $t$ dependent model assumes a sphere shape of the gold nucleus. The EIC kinematics are $\sqrt{s_{eN}} = 89$ GeV, $x = 0.008$, $y_l = 2.41$ with $\beta = 0.94$, $x_{\text{IP}} < 0.01$, $R = 0.4$.

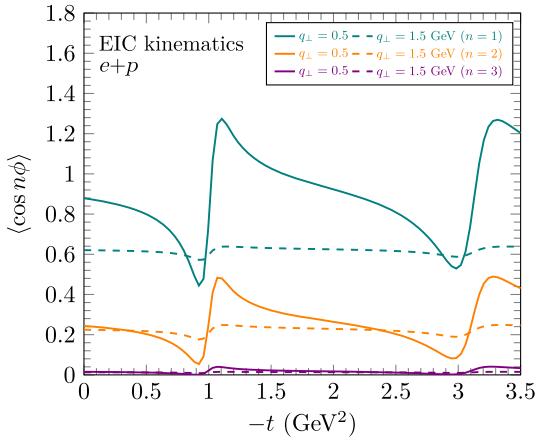


FIG. 16. The $t$ distribution of harmonics for diffractive lepton-jet production in $e + p$ collisions in the EIC kinematics, with the spherical density profile. Two different imbalanced momentum $q_\perp = 0.5$ GeV and $q_\perp = 1.5$ GeV have been chosen. The EIC kinematics are $\sqrt{s_{eN}} = 89$ GeV, $x = 0.008$, $y_l = 2.41$ with $\beta = 0.94$, $x_{\mathrm{IP}} < 0.01$, $R = 0.4$.

nature of this process. We will explain this behavior in the following discussion.

The $t$ distribution of diffractive scattering cross sections in nuclear and hadronic physics always exhibits a pulse shape [11,198,200], resembling the diffraction pattern in optics. We present the $t$ distribution of diffractive harmonics for $e + p$ collisions with a spherical proton in Fig. 16, with $q_\perp = 0.5$ GeV and $q_\perp = 1.5$ GeV. Since the sphere-shaped proton is circular in the transverse plane, the Fourier transform of a circle is the Bessel function of the first kind $J_1(r_p\Delta_\perp)$. The positions of the minima can be determined by zeros of the Bessel function $J_1(r_p\Delta_\perp)$ at

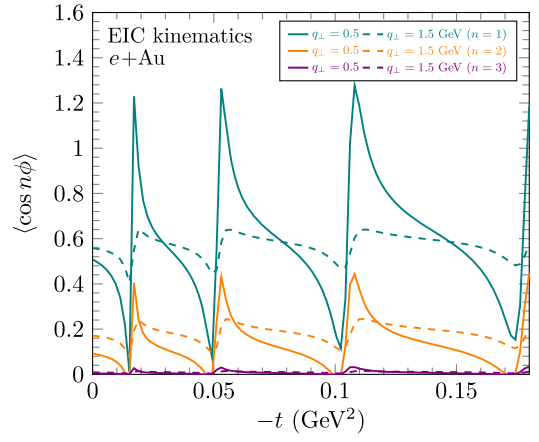


FIG. 17. The $t$ distribution of harmonics for diffractive lepton-jet production in $e + \mathrm{Au}$ collisions in the EIC kinematics, with the spherical density profile. Two different imbalanced momentum $q_\perp = 0.5$ GeV and $q_\perp = 1.5$ GeV have been chosen. The EIC kinematics are $\sqrt{s_{eN}} = 89$ GeV, $x = 0.008$, $y_l = 2.41$ with $\beta = 0.94$, $x_{\mathrm{IP}} < 0.01$, $R = 0.4$.

$r_p\Delta_\perp = 3.8, 7.0, 10.2, \ldots$ The first minina of Fig. 16 can be calculated as $-t = [3.8/r_p]^2 \approx 0.9$ GeV$^2$. Furthermore, we calculate the $t$ distribution of diffractive harmonics for $e + \mathrm{Au}$ collisions with a spherical gold nucleus in Fig. 17, considering $q_\perp = 0.5$ GeV and $q_\perp = 1.5$ GeV. The positions of minima are the same as those of the $t$ distribution for $J/\psi$ photoproduction [200], with the first minima as $-t = [3.8/r_A]^2 \approx 0.014$ GeV$^2$. In Fig. 15, the sharp peaks of the $q_\perp$ distribution of $e + \mathrm{Au}$ diffractive harmonics with $-t = 0.5$ GeV$^2$ arise from the divergent behavior at $-t = 0.5$ GeV$^2$, coinciding with one of the minima. In contrast, if the density profile were cylinderlike, the harmonics in Figs. 16 and 17 would be constant as $t$ varies.

The above calculation provides quantitative predictions to the future experimental studies on diffractive lepton-jet production at HERA and EIC.

## IV. CONCLUSION

In this paper, we propose novel observables for studying gluon saturation: harmonics and its nuclear modification factors of inclusive and diffractive lepton-jet correlation.

Using the small-$x$ framework, we derive the dominant contribution of the azimuthal-angle dependent lepton-jet correlation in the back-to-back limit by soft-gluon resummation. We obtain analytical expressions for the harmonics, which predicts the suppression of the harmonics with increasing of saturation scale $Q_s$. This behavior is confirmed by numerical calculation. Furthermore, we find that the QED radiation corrections to the harmonics is sizable, while negligible for the nuclear modification factor. These can be seen from expressions and numerical calculations. The striking difference in the nuclear modification factor between nonsaturation and saturation frameworks makes it a robust observable for distinguishing these two frameworks.

In addition, the parallel study on the diffractive lepton-jet production is carried out. Numerical calculations demonstrate that the diffractive harmonics are twice the value of the inclusive harmonics, while the nuclear modification factors are almost the same. These findings suggest that diffractive harmonics and their nuclear modification factors serve as sensitive observables for probing the gluon saturation phenomenon. In particular, $t$-dependent diffractive harmonics can distinguish different nuclear density profiles. Meanwhile, the $q_\perp$ dependence in this observable introduces an added kinematic dimension in addition to the $t$-dependence. Future measurements of the lepton-jet harmonics will complement previous studies in processes such as exclusive vector meson production [162–165] and deeply virtual Compton scattering [201–204] in terms of probing the proton and nucleus profiles.

For future studies, it would be intriguing to explore the lepton-jet corrections beyond the back-to-back limit in both

inclusive and diffractive DIS at small x through the complete next-to-leading order calculation.

## ACKNOWLEDGMENTS

We thank Feng Yuan and Heikki Mäntysaari for discussions. This work is supported by the CUHK-Shenzhen university development fund under the Grant No. UDF01001859. X. B. T. is supported by the Research Council of Finland, the Centre of Excellence in Quark Matter and under the European Union's Horizon 2020 research and innovation programme by the European Research Council (ERC, Grant Agreement No. ERC-2018-ADG-835105 YoctoLHC) and by the STRONG-2020 project (Grant Agreement No. 824093). The content of this article does not reflect the official opinion of the European Union and responsibility for the information and views expressed therein lies entirely with the authors.

[1] X.-B. Tong, B.-W. Xiao, and Y.-Y. Zhang, Phys. Rev. Lett. **130**, 151902 (2023).
[2] L. V. Gribov, E. M. Levin, and M. G. Ryskin, Phys. Rep. **100**, 1 (1983).
[3] A. H. Mueller and J.-w. Qiu, Nucl. Phys. **B268**, 427 (1986).
[4] A. H. Mueller, Nucl. Phys. **B335**, 115 (1990).
[5] L. D. McLerran and R. Venugopalan, Phys. Rev. D **49**, 2233 (1994).
[6] L. D. McLerran and R. Venugopalan, Phys. Rev. D **49**, 3352 (1994).
[7] L. D. McLerran and R. Venugopalan, Phys. Rev. D **50**, 2225 (1994).
[8] A. Morreale and F. Salazar, Universe **7**, 312 (2021).
[9] F. Gelis, E. Iancu, J. Jalilian-Marian, and R. Venugopalan, Annu. Rev. Nucl. Part. Sci. **60**, 463 (2010).
[10] E. Iancu and R. Venugopalan, The color glass condensate and high-energy scattering in QCD, in *Quark-Gluon Plasma 3*, edited by R. C. Hwa and X.-N. Wang (World Scientific, Singapore, 2004), pp. 249–3363.
[11] Y. V. Kovchegov and E. Levin, *Quantum Chromodynamics at High Energy*, Vol. 33 (Cambridge University Press, New York, 2013).
[12] J. L. Albacete and C. Marquet, Prog. Part. Nucl. Phys. **76**, 1 (2014).
[13] J.-P. Blaizot, Rep. Prog. Phys. **80**, 032301 (2017).
[14] F. Gelis and J. Jalilian-Marian, Phys. Rev. D **67**, 074019 (2003).
[15] R. Baier, A. Kovner, M. Nardi, and U. A. Wiedemann, Phys. Rev. D **72**, 094013 (2005).
[16] F. Dominguez, B.-W. Xiao, and F. Yuan, Phys. Rev. Lett. **106**, 022301 (2011).
[17] F. Dominguez, C. Marquet, B.-W. Xiao, and F. Yuan, Phys. Rev. D **83**, 105005 (2011).
[18] A. H. Mueller, B.-W. Xiao, and F. Yuan, Phys. Rev. D **88**, 114010 (2013).
[19] A. Dumitru, T. Lappi, and V. Skokov, Phys. Rev. Lett. **115**, 252301 (2015).
[20] A. Dumitru and V. Skokov, Phys. Rev. D **94**, 014030 (2016).
[21] D. Boer, P. J. Mulders, C. Pisano, and J. Zhou, J. High Energy Phys. 08 (2016) 001.
[22] A. Dumitru, V. Skokov, and T. Ullrich, Phys. Rev. C **99**, 015204 (2019).
[23] Y.-Y. Zhao, M.-M. Xu, L.-Z. Chen, D.-H. Zhang, and Y.-F. Wu, Phys. Rev. D **104**, 114032 (2021).
[24] R. Boussarie, H. Mäntysaari, F. Salazar, and B. Schenke, J. High Energy Phys. 09 (2021) 178.
[25] P. Taels, T. Altinoluk, G. Beuf, and C. Marquet, J. High Energy Phys. 10 (2022) 184.
[26] P. Caucal, F. Salazar, B. Schenke, and R. Venugopalan, J. High Energy Phys. 11 (2022) 169.
[27] P. Caucal, F. Salazar, B. Schenke, T. Stebel, and R. Venugopalan, J. High Energy Phys. 08 (2023) 062.
[28] P. Caucal, F. Salazar, B. Schenke, T. Stebel, and R. Venugopalan, arXiv:2308.00022.
[29] P. Caucal, F. Salazar, and R. Venugopalan, J. High Energy Phys. 11 (2021) 222.
[30] Y.-Y. Zhang and X.-N. Wang, Phys. Rev. D **105**, 034015 (2022).
[31] A. Metz and J. Zhou, Phys. Rev. D **84**, 051503 (2011).
[32] F. Dominguez, J.-W. Qiu, B.-W. Xiao, and F. Yuan, Phys. Rev. D **85**, 045003 (2012).
[33] R. Boussarie, A. V. Grabovsky, L. Szymanowski, and S. Wallon, J. High Energy Phys. 09 (2014) 026.
[34] R. Boussarie, A. V. Grabovsky, L. Szymanowski, and S. Wallon, J. High Energy Phys. 11 (2016) 149.
[35] F. Salazar and B. Schenke, Phys. Rev. D **100**, 034007 (2019).
[36] R. Boussarie, A. V. Grabovsky, L. Szymanowski, and S. Wallon, Phys. Rev. D **100**, 074020 (2019).
[37] H. Mäntysaari, N. Mueller, F. Salazar, and B. Schenke, Phys. Rev. Lett. **124**, 112301 (2020).
[38] D. Boer and C. Setyadi, Phys. Rev. D **104**, 074006 (2021).
[39] E. Iancu, A. H. Mueller, and D. N. Triantafyllopoulos, Phys. Rev. Lett. **128**, 202001 (2022).
[40] E. Iancu, A. H. Mueller, D. N. Triantafyllopoulos, and S. Y. Wei, J. High Energy Phys. 10 (2022) 103.
[41] Y. Hatta, B.-W. Xiao, and F. Yuan, Phys. Rev. Lett. **116**, 202301 (2016).
[42] T. Altinoluk, N. Armesto, G. Beuf, and A. H. Rezaeian, Phys. Lett. B **758**, 373 (2016).
[43] H. Mäntysaari, N. Mueller, and B. Schenke, Phys. Rev. D **99**, 074004 (2019).

[44] M. Fucilla, A. V. Grabovsky, E. Li, L. Szymanowski, and S. Wallon, J. High Energy Phys. 03 (2023) 159.
[45] B. Rodriguez-Aguilar, D. N. Triantafyllopoulos, and S. Y. Wei, Phys. Rev. D **107**, 114007 (2023).
[46] T. Altinoluk, G. Beuf, A. Czajka, and A. Tymowska, Phys. Rev. D **107**, 074016 (2023).
[47] T. Altinoluk, N. Armesto, and G. Beuf, Phys. Rev. D **108**, 074023 (2023).
[48] Y. Hagiwara, C. Zhang, J. Zhou, and Y.-j. Zhou, Phys. Rev. D **104**, 094021 (2021).
[49] L. Zheng, E. C. Aschenauer, J. H. Lee, and B.-W. Xiao, Phys. Rev. D **89**, 074037 (2014).
[50] F. Bergabo and J. Jalilian-Marian, Nucl. Phys. **A1018**, 122358 (2022).
[51] F. Bergabo and J. Jalilian-Marian, Phys. Rev. D **106**, 054035 (2022).
[52] E. Iancu and Y. Mulian, J. High Energy Phys. 07 (2023) 121.
[53] F. Bergabo and J. Jalilian-Marian, Phys. Rev. D **107**, 054036 (2023).
[54] I. Kolbé, K. Roy, F. Salazar, B. Schenke, and R. Venugopalan, J. High Energy Phys. 01 (2021) 052.
[55] D. Boer *et al.*, arXiv:1108.1713.
[56] A. Accardi *et al.*, Eur. Phys. J. A **52**, 268 (2016).
[57] R. Abdul Khalek *et al.*, Nucl. Phys. **A1026**, 122447 (2022).
[58] R. Abdul Khalek *et al.*, arXiv:2203.13199.
[59] R. Abir *et al.*, arXiv:2305.14572.
[60] A. H. Mueller, B.-W. Xiao, and F. Yuan, Phys. Rev. Lett. **110**, 082301 (2013).
[61] J. Jalilian-Marian and Y. V. Kovchegov, Phys. Rev. D **70**, 114017 (2004); **71**, 079901(E) (2005).
[62] D. Kharzeev, E. Levin, and L. McLerran, Nucl. Phys. **A748**, 627 (2005).
[63] C. Marquet, Nucl. Phys. **A796**, 41 (2007).
[64] K. Tuchin, Nucl. Phys. **A846**, 83 (2010).
[65] A. Dumitru and J. Jalilian-Marian, Phys. Rev. D **82**, 074023 (2010).
[66] K. Kutak and S. Sapeta, Phys. Rev. D **86**, 094043 (2012).
[67] A. van Hameren, P. Kotko, K. Kutak, and S. Sapeta, Phys. Lett. B **737**, 335 (2014).
[68] P. Kotko, K. Kutak, C. Marquet, E. Petreska, S. Sapeta, and A. van Hameren, J. High Energy Phys. 09 (2015) 106.
[69] A. van Hameren, P. Kotko, K. Kutak, C. Marquet, E. Petreska, and S. Sapeta, J. High Energy Phys. 12 (2016) 034; 02 (2019) 158(E).
[70] A. van Hameren, P. Kotko, K. Kutak, and S. Sapeta, Phys. Lett. B **795**, 511 (2019).
[71] A. van Hameren, P. Kotko, K. Kutak, and S. Sapeta, Phys. Lett. B **814**, 136078 (2021).
[72] A. van Hameren, H. Kakkad, P. Kotko, K. Kutak, and S. Sapeta, Eur. Phys. J. C **83**, 947 (2023).
[73] C. Marquet, E. Petreska, and C. Roiesnel, J. High Energy Phys. 10 (2016) 065.
[74] S. R. Klein and H. Mäntysaari, Nat. Rev. Phys. **1**, 662 (2019).
[75] E. Iancu and Y. Mulian, J. High Energy Phys. 03 (2021) 005.
[76] A. D. Bolognino, F. G. Celiberto, M. Fucilla, D. Y. Ivanov, and A. Papa, Phys. Rev. D **103**, 094004 (2021).
[77] M. A. Al-Mashad, A. van Hameren, H. Kakkad, P. Kotko, K. Kutak, P. van Mechelen, and S. Sapeta, J. High Energy Phys. 12 (2022) 131.
[78] P. Agostini, T. Altinoluk, and N. Armesto, Phys. Lett. B **840**, 137892 (2023).
[79] E. Iancu, A. H. Mueller, D. N. Triantafyllopoulos, and S. Y. Wei, Eur. Phys. J. C **83**, 1078 (2023).
[80] Y. Hagiwara, Y. Hatta, R. Pasechnik, M. Tasevsky, and O. Teryaev, Phys. Rev. D **96**, 034009 (2017).
[81] P. Kotko, K. Kutak, S. Sapeta, A. M. Stasto, and M. Strikman, Eur. Phys. J. C **77**, 353 (2017).
[82] S. Bhattacharya, A. Metz, V. K. Ojha, J.-Y. Tsai, and J. Zhou, Phys. Lett. B **833**, 137383 (2022).
[83] R. Boussarie, Y. Hatta, B.-W. Xiao, and F. Yuan, Phys. Rev. D **98**, 074015 (2018).
[84] J. L. Albacete and C. Marquet, Phys. Rev. Lett. **105**, 162301 (2010).
[85] A. Stasto, B.-W. Xiao, and F. Yuan, Phys. Lett. B **716**, 430 (2012).
[86] T. Lappi and H. Mantysaari, Nucl. Phys. **A908**, 51 (2013).
[87] E. Iancu and J. Laidet, Nucl. Phys. **A916**, 48 (2013).
[88] J. L. Albacete, G. Giacalone, C. Marquet, and M. Matas, Phys. Rev. D **99**, 014002 (2019).
[89] A. Stasto, S.-Y. Wei, B.-W. Xiao, and F. Yuan, Phys. Lett. B **784**, 301 (2018).
[90] J. Jalilian-Marian, Nucl. Phys. **A770**, 210 (2006).
[91] J. Jalilian-Marian and A. H. Rezaeian, Phys. Rev. D **86**, 034016 (2012).
[92] A. Stasto, B.-W. Xiao, and D. Zaslavsky, Phys. Rev. D **86**, 014009 (2012).
[93] A. H. Rezaeian, Phys. Rev. D **86**, 094016 (2012).
[94] E. Basso, V. P. Goncalves, J. Nemchik, R. Pasechnik, and M. Sumbera, Phys. Rev. D **93**, 034023 (2016).
[95] A. H. Rezaeian, Phys. Rev. D **93**, 094030 (2016).
[96] E. Basso, V. P. Goncalves, M. Krelina, J. Nemchik, and R. Pasechnik, Phys. Rev. D **93**, 094027 (2016).
[97] D. Boer, P. J. Mulders, J. Zhou, and Y.-j. Zhou, J. High Energy Phys. 10 (2017) 196.
[98] S. Benić and A. Dumitru, Phys. Rev. D **97**, 014012 (2018).
[99] V. P. Goncalves, Y. Lima, R. Pasechnik, and M. Šumbera, Phys. Rev. D **101**, 094019 (2020).
[100] S. Benić, O. Garcia-Montero, and A. Perkov, Phys. Rev. D **105**, 114052 (2022).
[101] D. Boer, Y. Hagiwara, J. Zhou, and Y.-j. Zhou, Phys. Rev. D **105**, 096017 (2022).
[102] F. Gelis and J. Jalilian-Marian, Phys. Rev. D **66**, 094014 (2002).
[103] A. Kovner and A. H. Rezaeian, Phys. Rev. D **90**, 014031 (2014).
[104] A. Kovner and A. H. Rezaeian, Phys. Rev. D **92**, 074045 (2015).
[105] C. Marquet, S.-Y. Wei, and B.-W. Xiao, Phys. Lett. B **802**, 135253 (2020).
[106] E. Akcakaya, A. Schäfer, and J. Zhou, Phys. Rev. D **87**, 054010 (2013).
[107] C. Marquet, C. Roiesnel, and P. Taels, Phys. Rev. D **97**, 014004 (2018).

[108] W.-L. Ju and M. Schönherr, J. High Energy Phys. 02 (2023) 075.
[109] I. Ganguli, A. van Hameren, P. Kotko, and K. Kutak, Eur. Phys. J. C **83**, 868 (2023).
[110] X. Liu, F. Ringer, W. Vogelsang, and F. Yuan, Phys. Rev. Lett. **122**, 192003 (2019).
[111] X. Liu, F. Ringer, W. Vogelsang, and F. Yuan, Phys. Rev. D **102**, 094022 (2020).
[112] M. Arratia, Z.-B. Kang, A. Prokudin, and F. Ringer, Phys. Rev. D **102**, 074015 (2020).
[113] Z.-B. Kang, K. Lee, D. Y. Shao, and F. Zhao, J. High Energy Phys. 11 (2021) 005.
[114] M. Arratia, Z.-B. Kang, S. J. Paul, A. Prokudin, F. Ringer, and F. Zhao, Phys. Rev. D **107**, 094036 (2023).
[115] Z.-B. Kang, X. Liu, S. Mantry, and D. Y. Shao, Phys. Rev. Lett. **125**, 242003 (2020).
[116] W. Yang and X. Yang, Nucl. Phys. **B990**, 116181 (2023).
[117] W. Yang, Phys. Rev. D **108**, 056022 (2023).
[118] H. Abramowicz and A. Caldwell, Rev. Mod. Phys. **71**, 1275 (1999).
[119] V. Andreev *et al.* (H1 Collaboration), Phys. Rev. Lett. **128**, 132002 (2022).
[120] M. Arratia, Y. Song, F. Ringer, and B. V. Jacak, Phys. Rev. C **101**, 065204 (2020).
[121] Y. Hatta, B.-W. Xiao, F. Yuan, and J. Zhou, Phys. Rev. D **104**, 054037 (2021).
[122] Y. Hatta, B.-W. Xiao, F. Yuan, and J. Zhou, Phys. Rev. Lett. **126**, 142001 (2021).
[123] C. Marquet, B.-W. Xiao, and F. Yuan, Phys. Lett. B **682**, 207 (2009).
[124] B.-W. Xiao and F. Yuan, Phys. Rev. D **82**, 114009 (2010).
[125] B.-W. Xiao and F. Yuan, Phys. Rev. Lett. **105**, 062001 (2010).
[126] S. Catani, M. Grazzini, and A. Torre, Nucl. Phys. **B890**, 518 (2014).
[127] S. Catani, M. Grazzini, and H. Sargsyan, J. High Energy Phys. 06 (2017) 017.
[128] Y. Hatta, B.-W. Xiao, and F. Yuan, Phys. Rev. D **106**, 094015 (2022).
[129] A. Berera and D. E. Soper, Phys. Rev. D **53**, 6162 (1996).
[130] A. Hebecker, Nucl. Phys. **B505**, 349 (1997).
[131] W. Buchmuller, T. Gehrmann, and A. Hebecker, Nucl. Phys. **B537**, 477 (1999).
[132] K. J. Golec-Biernat and M. Wusthoff, Phys. Rev. D **60**, 114023 (1999).
[133] F. Hautmann, Z. Kunszt, and D. E. Soper, Nucl. Phys. **B563**, 153 (1999).
[134] F. Hautmann and D. E. Soper, Phys. Rev. D **63**, 011501 (2001).
[135] K. J. Golec-Biernat and M. Wusthoff, Eur. Phys. J. C **20**, 313 (2001).
[136] H. Mäntysaari, Rep. Prog. Phys. **83**, 082201 (2020).
[137] L. Frankfurt, V. Guzey, A. Stasto, and M. Strikman, Rep. Prog. Phys. **85**, 126301 (2022).
[138] S. Munier and A. Shoshi, Phys. Rev. D **69**, 074022 (2004).
[139] C. Marquet, Phys. Rev. D **76**, 094017 (2007).
[140] H. Kowalski, T. Lappi, C. Marquet, and R. Venugopalan, Phys. Rev. C **78**, 045201 (2008).
[141] M. S. Kugeratski, V. P. Goncalves, and F. S. Navarra, Eur. Phys. J. C **46**, 413 (2006).
[142] E. R. Cazaroto, F. Carvalho, V. P. Goncalves, and F. S. Navarra, Phys. Lett. B **671**, 233 (2009).
[143] Y. V. Kovchegov and E. Levin, Nucl. Phys. **B577**, 221 (2000).
[144] Y. V. Kovchegov, Phys. Lett. B **710**, 192 (2012).
[145] A. Kovner, M. Lublinsky, and H. Weigert, Phys. Rev. D **74**, 114023 (2006).
[146] M. Lublinsky, Phys. Lett. B **735**, 200 (2014).
[147] E. Levin and M. Lublinsky, Eur. Phys. J. C **22**, 647 (2002).
[148] E. Levin and M. Lublinsky, Phys. Lett. B **521**, 233 (2001).
[149] E. Levin and M. Lublinsky, Nucl. Phys. **A712**, 95 (2002).
[150] Y. Hatta, E. Iancu, C. Marquet, G. Soyez, and D. N. Triantafyllopoulos, Nucl. Phys. **A773**, 95 (2006).
[151] Y. Hatta, Proc. Sci., DIFF2006 (**2006**) 037.
[152] C. Contreras, E. Levin, R. Meneses, and I. Potashnikova, Eur. Phys. J. C **78**, 699 (2018).
[153] D. Bendova, J. Cepila, J. G. Contreras, t. V. P. Gonçalves, and M. Matas, Eur. Phys. J. C **81**, 211 (2021).
[154] A. D. Le, Phys. Rev. D **104**, 014014 (2021).
[155] G. Beuf, H. Hänninen, T. Lappi, Y. Mulian, and H. Mäntysaari, Phys. Rev. D **106**, 094014 (2022).
[156] T. Lappi, A. D. Le, and H. Mäntysaari, Phys. Rev. D **108**, 114023 (2023).
[157] J. Singh and T. Toll, Comput. Phys. Commun. **292**, 108872 (2023).
[158] H. Mäntysaari and B. Schenke, Phys. Rev. D **94**, 034042 (2016).
[159] H. Mäntysaari and B. Schenke, Phys. Rev. Lett. **117**, 052301 (2016).
[160] H. Mäntysaari, K. Roy, F. Salazar, and B. Schenke, Phys. Rev. D **103**, 094026 (2021).
[161] H. Mäntysaari and J. Penttala, J. High Energy Phys. 08 (2022) 247.
[162] A. Kumar and T. Toll, Phys. Rev. D **105**, 114011 (2022).
[163] S. Demirci, T. Lappi, and S. Schlichting, Phys. Rev. D **106**, 074025 (2022).
[164] H. Mäntysaari and J. Penttala, Phys. Rev. D **105**, 114038 (2022).
[165] H. Mäntysaari, B. Schenke, C. Shen, and W. Zhao, Phys. Rev. Lett. **131**, 062301 (2023).
[166] L. D. McLerran and R. Venugopalan, Phys. Rev. D **59**, 094002 (1999).
[167] R. Venugopalan, Acta Phys. Pol. B **30**, 3731 (1999).
[168] A. H. Mueller, Nucl. Phys. **B558**, 285 (1999).
[169] B.-W. Xiao, F. Yuan, and J. Zhou, Nucl. Phys. **B921**, 104 (2017).
[170] G. A. Chirilli, B.-W. Xiao, and F. Yuan, Phys. Rev. Lett. **108**, 122301 (2012).
[171] G. A. Chirilli, B.-W. Xiao, and F. Yuan, Phys. Rev. D **86**, 054005 (2012).
[172] G. Parisi and R. Petronzio, Nucl. Phys. **B154**, 427 (1979).
[173] J. C. Collins and D. E. Soper, Nucl. Phys. **B197**, 446 (1982).
[174] J. C. Collins, D. E. Soper, and G. F. Sterman, Nucl. Phys. **B250**, 199 (1985).
[175] Y. Shi, L. Wang, S.-Y. Wei, and B.-W. Xiao, Phys. Rev. Lett. **128**, 202302 (2022).
[176] T. Liu, W. Melnitchouk, J.-W. Qiu, and N. Sato, Phys. Rev. D **104**, 094033 (2021).

[177] T. Liu, W. Melnitchouk, J.-W. Qiu, and N. Sato, J. High Energy Phys. 11 (2021) 157.
[178] T.-J. Hou *et al.*, Phys. Rev. D **103**, 014013 (2021).
[179] K. J. Eskola, P. Paakkinen, H. Paukkunen, and C. A. Salgado, Eur. Phys. J. C **82**, 413 (2022).
[180] P. Sun, J. Isaacson, C. P. Yuan, and F. Yuan, Int. J. Mod. Phys. A **33**, 1841006 (2018).
[181] A. Prokudin, P. Sun, and F. Yuan, Phys. Lett. B **750**, 533 (2015).
[182] K. J. Golec-Biernat and M. Wusthoff, Phys. Rev. D **59**, 014017 (1998).
[183] I. Balitsky, Nucl. Phys. **B463**, 99 (1996).
[184] Y. V. Kovchegov and H. Weigert, Nucl. Phys. **A789**, 260 (2007).
[185] Y. V. Kovchegov, Phys. Rev. D **60**, 034008 (1999).
[186] Y. V. Kovchegov and H. Weigert, Nucl. Phys. **A784**, 188 (2007).
[187] J. L. Albacete, N. Armesto, J. G. Milhano, P. Quiroga-Arias, and C. A. Salgado, Eur. Phys. J. C **71**, 1705 (2011).
[188] K. J. Golec-Biernat, L. Motyka, and A. M. Stasto, Phys. Rev. D **65**, 074037 (2002).
[189] J. L. Albacete and Y. V. Kovchegov, Phys. Rev. D **75**, 125021 (2007).
[190] I. Balitsky, Phys. Rev. D **75**, 014001 (2007).
[191] E. Gardi, J. Kuokkanen, K. Rummukainen, and H. Weigert, Nucl. Phys. **A784**, 282 (2007).
[192] I. Balitsky and G. A. Chirilli, Phys. Rev. D **77**, 014019 (2008).
[193] J. Berger and A. Stasto, Phys. Rev. D **83**, 034015 (2011).
[194] H. Fujii and K. Watanabe, Nucl. Phys. **A915**, 1 (2013).
[195] T. Lappi and H. Mäntysaari, Phys. Rev. D **88**, 114020 (2013).
[196] F. Torales-Acosta (private communication).
[197] M. Anselmino, V. Barone, and A. Kotzinian, Phys. Lett. B **699**, 108 (2011).
[198] V. Barone and E. Predazzi, *High-Energy Particle Diffraction*, Texts and Monographs in Physics Vol. 565 (Springer-Verlag, Berlin Heidelberg, 2002).
[199] M. Diehl and S. Sapeta, Eur. Phys. J. C **41**, 515 (2005).
[200] A. Caldwell and H. Kowalski, Phys. Rev. C **81**, 025203 (2010).
[201] H. Kowalski, L. Motyka, and G. Watt, Phys. Rev. D **74**, 074016 (2006).
[202] M. V. T. Machado, Eur. Phys. J. C **59**, 769 (2009).
[203] T. Toll and T. Ullrich, Phys. Rev. C **87**, 024913 (2013).
[204] Y. Hatta, B.-W. Xiao, and F. Yuan, Phys. Rev. D **95**, 114026 (2017).